Journal of Volcanology and Geothermal Research 369 (2019) 121–144

Contents lists available at ScienceDirect

Journal of Volcanology and Geothermal Research

journal homepage: www.elsevier.com/locate/jvolgeores

Basalt, Unveiling Fluid-filled Fractures, Inducing Sediment Intra-void Transport, Ephemerally: Examples from Katla 1918

Jacqueline Owen [a,*], Thomas Shea [b], Hugh Tuffen [a]

[a] Lancaster Environment Centre, Lancaster University, Lancaster LA1 4YQ, UK
[b] Department of Geology and Geophysics, SOEST, University of Hawaii, Honolulu, HI 96822, USA

ARTICLE INFO

Article history:
Received 13 April 2018
Received in revised form 31 October 2018
Accepted 2 November 2018
Available online 07 November 2018

Keywords:
Degassing
Vesicles
Open-system degassing
Phreatomagmatic
Tuffisite veins
Katla

ABSTRACT

This article documents textures within basaltic Katla 1918 pyroclasts, where particle-filled fractures and bubbles have been observed. These features are analogous to tuffisite veins; particle-filled fractures which represent the preserved remains of transient degassing pathways in shallow conduits.

Such fractures have long been considered restricted to high viscosity silicic melts. However, through BSE images and compositional maps, we have identified similar tuffisite-like features in crystal-poor basalt pyroclasts from the 1918 CE subglacial eruption of Katla, Iceland (K1918). Clast textures record transient mobility of juvenile/lithic particles, melt droplets and gas through magmatic fractures and connected vesicles. Key evidence includes (1) the presence of variably sintered fine-ash particles within variably healed fractures and vesicles (present in >80% of clasts analysed), (2) compositional maps that reveal the presence of foreign particles within preserved and healed permeable pathways, and (3) lower vesicularities immediately surrounding 'fracture' walls, suggestive of diffusive volatile loss into a permeable network.

The 1918 CE eruption of Katla occurred under a thick glacier, however the ice was quickly breached, owing partly to the explosive nature of the eruption. We propose that the formation and preservation of these transient permeable networks have been facilitated by rapid decompression of a relatively volatile-rich magma, in a confined subglacial environment, with combined magmatic and phreatomagmatic fragmentation, followed by rapid quenching by meltwater.

Tuffisite veins in rhyolite demonstrate repeated fracture-healing cycles, which drive incremental release of overpressured gas and help to defuse explosive eruptions. Interestingly, the permeable network at Katla failed to defuse the 1918 CE eruption, which involved a particularly violent subglacial eruptive phase. It is unclear whether this demonstrates an inability of mafic tuffisite-like features to efficiently degas magma (perhaps owing to the especially transient nature of permeable pathways in low viscosity magmas) or an ability to enhance fragmentation by providing infiltration pathways for external water. The latter scenario may explain the rapid melting of the overlying glacier as the large surface area-to-volume ratio of fractured magma would allow rapid heat transfer.

Nevertheless, we document a previously unrecognised texture in basaltic magmas. It is intriguing why it has not, to the best of our knowledge, been documented elsewhere. Have these permeable pathways been overlooked in the past (e.g. mistaken for bad sample preparation or not noticed without high magnification BSE images) and are in fact a widespread phenomenon in subglacial (and other?) basalts; or do our samples in fact represent a rarely preserved texture? Either way, they offer a new insight into the degassing and fragmentation of subglacial basalt.

1. Introduction

Due to the ability of volcanic gases to rapidly expand at low pressure, volatiles are often considered the driving force for explosive volcanism (Sparks, 1978; Moore et al., 1998; Blundy et al., 2006), with violent fragmentation typically fuelled by high volatile contents and closed system degassing (i.e. where the volatiles remain trapped within the magma) (Anderson and Fink, 1989; Hoblitt and Harmon, 1993; Anderson et al., 1995; Martel et al., 1998; Villemant and Boudon, 1998; Villemant and Boudon, 1999; Villemant et al., 2003; Adams et al., 2006; Villemant et al., 2008; Humphreys et al., 2009; Owen et al., 2013a). Transitions to effusive volcanism are often characterised by a shift towards open system degassing behaviour, where volatiles are able to efficiently outgas from the magma (Jaupart and Allègre, 1991; Jaupart, 1998; Namiki and Manga, 2008; Owen et al., 2013b).

* Corresponding author.
E-mail address: j.owen2@lancaster.ac.uk (J. Owen).

https://doi.org/10.1016/j.jvolgeores.2018.11.002
0377-0273/

Magma outgassing occurs according to different mechanisms that strongly depend on melt composition (Vergniolle and Jaupart, 1986; Houghton and Gonnermann, 2008). The low viscosity of basalt, coupled with high volatile diffusivities in basaltic melts, enables bubbles to rapidly grow and buoyantly rise through the magma column, allowing efficient magma-gas separation and open-system degassing (Wilson, 1980; Vergniolle and Jaupart, 1986; Edmonds and Gerlach, 2007; Menand and Phillips, 2007; Houghton and Gonnermann, 2008). In contrast, the high viscosity and lower volatile diffusivities in silicic melts hinder both bubble growth (Proussevitch and Sahagian, 1996) and melt-bubble decoupling (Sparks, 1978). However, high-Si magmas can still experience open system degassing by becoming permeable, either with connected bubbles acting as a pathway for gas to flow (Eichelberger et al., 1986; Westrich and Eichelberger, 1994; Klug and Cashman, 1996; Namiki and Manga, 2008), and/or by the creation of tuffisite veins, permeable gas and ash filled fracture networks that temporarily exist within the magma conduit (Sparks, 1997; Tuffen et al., 2003; Saubin et al., 2016; Farquharson et al., 2017).

Magma fracturing and tuffisite vein formation are currently thought to be limited to high viscosity magmas such as rhyolites (Tuffen et al., 2003; Castro et al., 2012; Saubin et al., 2016), crystal-rich andesites (Kolzenburg et al., 2012; Plail et al., 2014; Kendrick et al., 2016) and dacites (Nakada et al., 2005; Noguchi et al., 2008; Gaunt et al., 2014). Tuffisite veins within conduits are proposed to form when highly viscous magma experiences failure either due to gas overpressure or shear fracture within the glass transition (Tg) interval. These fractures then act as a pathway for gas and fragmented particles that eventually obstruct the vein. Subsequent welding of these particles results in vein healing and permeable pathway occlusion, leading to repressurisation (Tuffen et al., 2003). Slow crystallisation rates in rhyolite allow prolonged magma residence in the glass transition interval (hours or days), providing sufficient time for repeated fracture-healing episodes within crystal-poor melt, and creating superimposed generations of tuffisite veins within flow banded glass (Tuffen et al., 2003; Gonnermann and Manga, 2005).

In contrast, the low viscosity of basalt means that repeated episodes of fracturing and healing within the conduit are unlikely. Inherently, it is much harder to fragment/fracture basaltic magma at eruptive temperatures (Papale, 1999; Giordano and Dingwell, 2003) without decreasing temperature, increasing crystallinity (Giordano and Dingwell, 2003; Houghton and Gonnermann, 2008; Namiki and Manga, 2008) and/or by invoking rapid decompression and/or magma-water interaction (Giordano and Dingwell, 2003). These processes will all hinder subsequent sintering, as rapid cooling would serve to quench the magma and high crystallinities lower the available melt fraction. Therefore, even if fracturing were able to occur in a crystal-free basaltic melt, rapid crystallisation will limit its residence time in the Tg interval, allowing little time for sintering, vein healing or repeated fragmentation cycles (Tuffen et al., 2003). It is perhaps not surprising that, to our knowledge, there is no documented evidence of tuffisite-like features within basaltic magma.

In this paper we present some of the first observations supporting transient particle transport and sintering within permeable pathways (fractures, connected vesicles and inter-clast void spaces) in a high-temperature, crystal-poor basalt. This process likely preceded powerful hydromagmatic fragmentation, emphasising a need to better understand the influence of open-system degassing and clast recycling in basaltic eruptions.

2. Materials and methods

2.1. Geological background and sampling

Samples were collected within deposits from the 1918 CE VEI 4 (Smithsonian, 2016) subglacial basaltic eruption of Katla (K1918) in South Iceland (Fig. 1a). The eruption took just 2 h to melt through ~400 m of overlying ice (Mýrdalsjökull glacier), after which both an ash plume and a jökulhlaup (glacial flood) were observed (Tómasson, 1996; Sturkell et al., 2010). The plume was 14 km high, and deposited ash over 50,000 km^2 of land (Larsen, 2010). The jökulhlaup transported 0.7–1.6 km^3 of tephra (Larsen, 2000), with an inferred peak discharge rate of >300,000 $m^3\ s^{-1}$ (Tómasson, 1996), making it the 14th most powerful flood of the Quaternary (last 2.6 million years) (O'Connor and Costa, 2004). Both the jökulhlaup and the extreme melting rate of the glacier were exceptional and cannot be readily explained by existing models of convective magma-ice heat transfer (Gudmundsson et al., 1997; Hoskuldsson and Sparks, 1997; Wilson and Head, 2002; Gudmundsson, 2013; Woodcock et al., 2014; Woodcock et al., 2015; Woodcock et al., 2016).

Samples characterised in this study were collected from both the air-fall and the jökulhlaup deposit. Wind blew ash from the eruption plume in many directions but predominantly to the NE (Larsen, 2010; Larsen et al., 2014), with ~300 g m^{-2} reaching North Iceland (Larsen et al., 2014). However, the ash was poorly preserved following the eruption. Nevertheless, K1918 ash can be found in select soil horizons around Katla (Óladóttir et al., 2005; Óladóttir et al., 2008), and the thickest deposit is observed as a layer in the Mýrdalsjökull ice, which is now being exhumed (Gudmundsson, 2013, pers. comm).

The K1918 jökulhlaup deposit has been well characterised by a variety of studies (e.g. Maizels, 1992; Maizels, 1993; Tómasson, 1996; Duller et al., 2008; Russell et al., 2010). Maizels (1992) identified four units; 1: a basal unit of massive gravels and imbricated clast-supported gravels that represents rising flow, overlain by 2: massive pumice granules interpreted to be part of a flow surge, overlain by 3: trough cross-bedded pumice granules, and finally 4: horizontally bedded pumice granules and pumice sands, with the top two units representing more fluid waning stages of the jökulhlaup. The deposit is ~12 m thick in proximal regions, decreasing to 4 m thick at the coast, some 18 km away (Maizels, 1992).

Air-fall tephra was collected from Sólheimajökull glacier (Fig. 1a) where a ~40-cm thick layer of typically sub-cm clasts are preserved in the ice (Fig. 1b). These samples are prefixed "Sol". Jökulhlaup samples (prefixed "Mul") were collected from the banks of the Múlakvísl river, where river downcutting has exposed a clear vertical cross-section through the deposit (Fig. 1c). In both settings multiple locations were sampled, which is denoted by the second part of the sample name. At Múlakvísl we focussed on a 3 m high exposure (Fig. 1a, c). In both locations, there were multiple layers, each of which was sampled. The layer makes up the third part of the sample name. For the air-fall tephra six layers were documented and labelled A–F (Fig. 1b). The observed stratigraphy at the jökulhlaup deposit matches the units described in Maizels (1992), Duller et al. (2008) and Russell et al. (2010) but with only units 2–4 exposed (Fig. 1c). The lower and upper half of unit 3 appeared more lithic- and juvenile-rich respectively and was separated by a vein. As a result, we collected two samples from unit 3 and labelled them 3a and 3b respectively (Fig. 1c).

Grain size distributions revealed that for the samples collected, the largest clast sizes typically fell within the −3 to −4 φ category (8–16 mm) and had a peak at the −1 to −2 φ category (2–4 mm). Typical air fall samples had a second modal group with a high proportion <125 μm (>3 φ). However, it should be noted that, in both settings, the grain size distribution is probably a reflection of the history of transportation and potentially re-mobilisation, rather than the true volcanic deposition. This is especially true of the jökulhlaup deposit where it is thought that the majority of the fines and most of the early material was washed out to sea (Duller et al., 2008). Nevertheless, for each key sample, four representative 8–16 mm and nine 2–4 mm clasts were chosen, numbered and made into thin sections. The clast size and number make up the fourth and fifth (final) parts of the sample name, respectively. In total 100 clasts of this size were thin sectioned and of these, 26 representative clasts (9 air-fall and 17 jökulhlaup samples) were chosen for backscatter imaging.

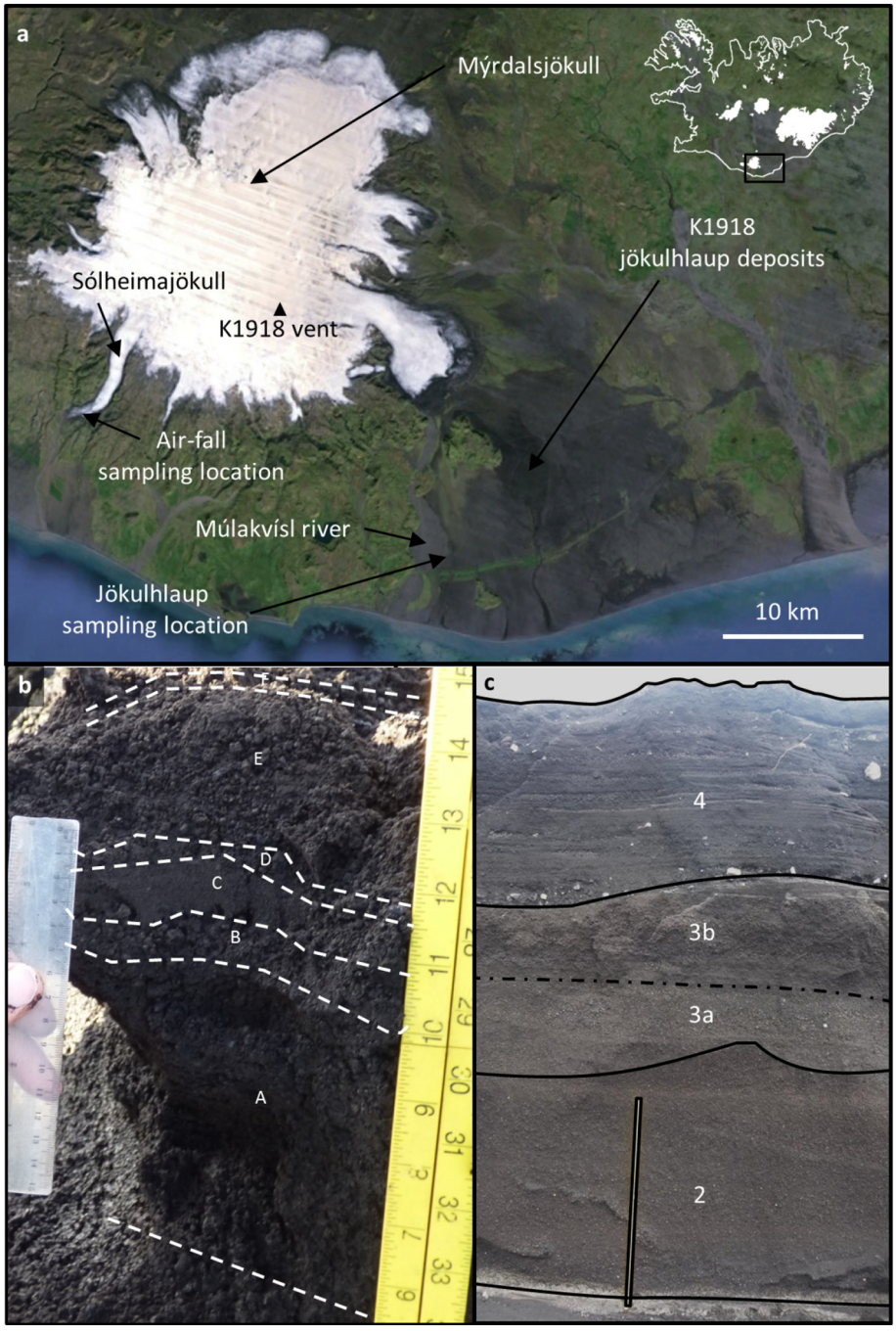

Fig. 1. (a) Map of the Katla area showing the sampling locations with the inlet showing the position in South Iceland; (b) Cross-section through the air-fall deposit on Sólheimajökull glacier showing units A–F; (c) Cross-section of the jökulhlaup deposit at Múlakvísl showing the different units sampled (units 2 to 4 from Duller et al. (2008)) with a meter rule for scale.

Thin sections were also made of the 250–500 μm clast size to supplement the geochemistry data.

Each sample name therefore, has the following format 1) environmental setting 2) location number, 3) layer/unit reference, 4) clast size, 5) clast number.

2.2. Geochemistry and imaging (EPMA)

A Field-emission JEOL Hyperprobe JXA-8500F Electron Probe Micro-Analyser (EPMA) at the University of Hawaii was used to acquire (a) back-scattered electron (BSE) images, (b) compositional (X-ray distribution) maps and (c) spot analyses. Accelerating voltages of 15, 20 and 20 keV and beam currents of 10, 30–50, and 10 nA were used for (a), (b) and (c) respectively. Spot sizes of 1 μm, 2 μm and 10 μm were used for Fe-Ti oxides, K-rich particles and matrix glass, respectively. On-peak count times of 30 s were used for Si, Al, Fe, Mn, Na, K, P, and 65–70 s for Al, Mg, Ca, and Cl. Time-dependent intensity corrections were used for glass analyses when significant Na loss or Si gains were detected (e.g. Shea et al., 2014).

To assess compositional heterogeneity and relative element abundances in select samples, compositional maps of Fe, Ca and K were obtained using three of the five spectrometers and dwell times of 40–45 msec/pixel. Raw data was used to make single 2D intensity matrices, which were then combined as individual channels into a single RGB composite image. The other two spectrometers measured S and either F or Na. Intensity matrices for all measured elements are provided in Appendix 1 (Figs. A1–A3).

Spot analyses were mainly performed on magnetite and ilmenite crystals for geothermometry (see Section 2.3). A limited number of glass analyses were also acquired and compared to EPMA data collected from the University of Edinburgh. There, >200 glass measurements were made on >50 different air-fall and jökulhlaup clasts. All analyses were carried out at 15 kV with a 5 μm spot size. Beam currents of 2 and 80 nA were used for major and minor/trace elements respectively as per Hayward (2011). Analyses with totals <97 wt% and those with a clear influence of crystals were rejected.

2.3. Estimating eruption temperature (geothermometry)

To better constrain the physical parameters of the melt (e.g. viscosity and rates of diffusion and sintering) oxide geothermometry was used to estimate the magma eruptive temperature. Using the method described in Section 2.2, 61 measurements were made of magnetite and ilmenite crystals within both jökulhlaup and air-fall samples. These were converted into temperatures using the Fe-Ti oxide geothermobarometer model of Ghiorso and Evans (2008). Measurements were rejected if either SiO_2 exceeded 1 wt%, as this may reflect mixed analyses with surrounding glass, or if they failed the equilibrium test of Bacon and Hirschmann (1988).

2.4. Glass H_2O content (FTIR)

The glass water contents of five clasts (one air-fall and four jökulhlaup) were measured using Fourier Transform Infrared Spectroscopy (FTIR). A Thermo Nicolet IR interferometer, with KBr beamsplitter, Continuum Analytical microscope and MCT-A detector were used at Lancaster University. Each measurement (including background analyses) constituted 256 spectra collected at 4 cm^{-1} resolution over the range 600–5500 cm^{-1}. A minimum of ten measurements were taken per sample with a 100 × 100 μm aperture.

H_2O contents (C) were determined using the Beer-Lambert law (e.g. Stolper, 1982)

$$C = \frac{M_w A}{d\rho\epsilon} \quad (1)$$

where M_w is the molecular weight of water (18.02 g mol^{-1}), A is peak height, d is sample thickness (in cm), ρ is density (2770 g l^{-1} estimated using the density calculator of Bottinga and Weill (1970) and a representative composition of K1918 basalt taken from Óladóttir et al. (2008)), and ε is the absorption coefficient (l mol^{-1} cm^{-1}).

Total H_2O (H_2O_t) concentrations were determined using the absorption peak at 3550 cm^{-1} and an absorption coefficient of 63 l mol^{-1} cm^{-1} (Dixon et al., 1988). Sample thickness was determined using a Mitutoyo digital displacement gauge accurate to ±3 μm.

The characteristic double CO_3^{2-} peaks (1515 and 1435 cm^{-1}) and the molecular H_2O (H_2O_m) peak at 1630 cm^{-1} were indiscernible, suggestive of very low CO_2 and H_2O_m concentrations. As post quenching hydration favours H_2O_m (Yokoyama et al., 2008; Denton et al., 2009), it is unlikely that our K1918 samples have undergone this process.

3. Results

3.1. Overview of clasts

Clasts tend to be brown, black (or a mixture of the two) and contain sparse phenocrysts. The brown material (e.g. Figs. 2b, 3, 4bii) is clear glass (sideromelane), with few microlites (typically 5–25% for air-fall and <5% for jökulhlaup clasts), in contrast to the black (tachylite) material (e.g. Fig. 4aii), which is relatively microlite-rich (~30–70%), opaque, and contains bubbles that are largely obscured in plane-polarised light (ppl) microscopy. Air-fall clasts are typically 40–50% vesicular whilst jökulhlaup clasts are ~60–75% vesicular, with a large number of small bubbles (Owen et al., 2017). Bubble and microlite textures are often locally heterogeneous throughout each clast. Many clasts contain fractures, connected bubbles and textural evidence of sintering, which are particularly well preserved in the jökulhlaup samples (see sections below). Note that in this paper, we will use the term 'sintering' in reference to a texture that shows any of the stages of sintering from contact point fusing to full coalescence and compaction into a continuous solid mass. In addition to the brown and black clasts, there is a small percentage of pale/clear lithic clasts that are largely void of both phenocrysts and vesicles.

3.2. Fractures

Most clasts contain fractures that have either a ragged, sharp angular appearance (Fig. 2) or a smoother, more rounded morphology (Fig. 3). Fractures observed are typically millimetric in length and tens to hundreds of μm wide, however observations were limited by clast size (<16 mm). It is common for the fractures to be partially filled by ash particles. Ash also occurs within neighbouring vesicles connected to the fractures, but tends to be absent from nearby isolated bubbles (e.g. Fig. 2c). The fracture- and vesicle-occupying particles shall herein be referred to as 'particles', and the host as 'clast' to avoid confusion. The fracture-hosted particles are typically of μm scale but can reach 250 μm in the largest fractures. They are predominantly composed of vesicle-free basalt (both sideromelane and tachylite), but lithics are also present, and some of the larger particles can contain vesicles. The particles tend to be either angular or well rounded, and sometimes appear welded to nearby surfaces (Figs. 4, 5a).

As can be seen in Fig. 4, the particle-filled fractures, which are fairly evident in the BSE images on the left, are not at all clear in the ppl images on the right. This is especially true for the tachylite sample (Fig. 4a) where the opaqueness of the matrix makes the feature (and many of the bubbles) invisible in ppl (Fig. 4aii). This is not only true for particle filled fractures but also particle filled bubbles and in fact most examples of sintering.

Particles within fractures and bubbles are noticeably vesicle-poor compared to their host clasts, likely reflecting their grain size being smaller than the predominant bubble size (Fig. 4ai). Most particles are in fact void of vesicles. There are, however, some exceptions, for example the larger fracture-filling particles in Fig. 4b share similar bubble contents and textures to the melt immediately surrounding the fracture. In turn, this area is less vesicular, with typically smaller and less abundant bubbles than material >100 μm away.

Compositional mapping of a particle-filled fracture (Fig. 5a) shows that most particles have compositions similar to the surrounding microlite-free host basaltic melt (sideromelane). However, the fracture also contains a significant percentage of K-rich (blue) particles (Fig. 5a), which are mostly also Na-rich, although some are Na-poor (Appendix 1; Fig. A1). There is also a large Na-rich phenocryst (dark green in Fig. 5a) and microlites of this composition within some of the K-rich particles. These K/Na-rich particles likely represent fragments of silicic glass, alkali feldspar, and albitic plagioclase from a more evolved magma. Particles are predominantly subangular, but a significant proportion, especially of sideromelane, display rounded morphologies. Some rounded sideromelane particles have viscously deformed around K-rich particles, whilst others are sintered to the fracture walls, with the former boundaries expressed by oxide microlite chains (pink in Fig. 5a). Additional microlite chains occur in the basaltic glass surrounding the fracture, outlining domains that are similar in size and shape to the particles within the fracture. These microlite chains are S-enriched (Fig. A1). Also present in the surrounding glass are a few additional K-rich fragments and partially collapsed vesicles.

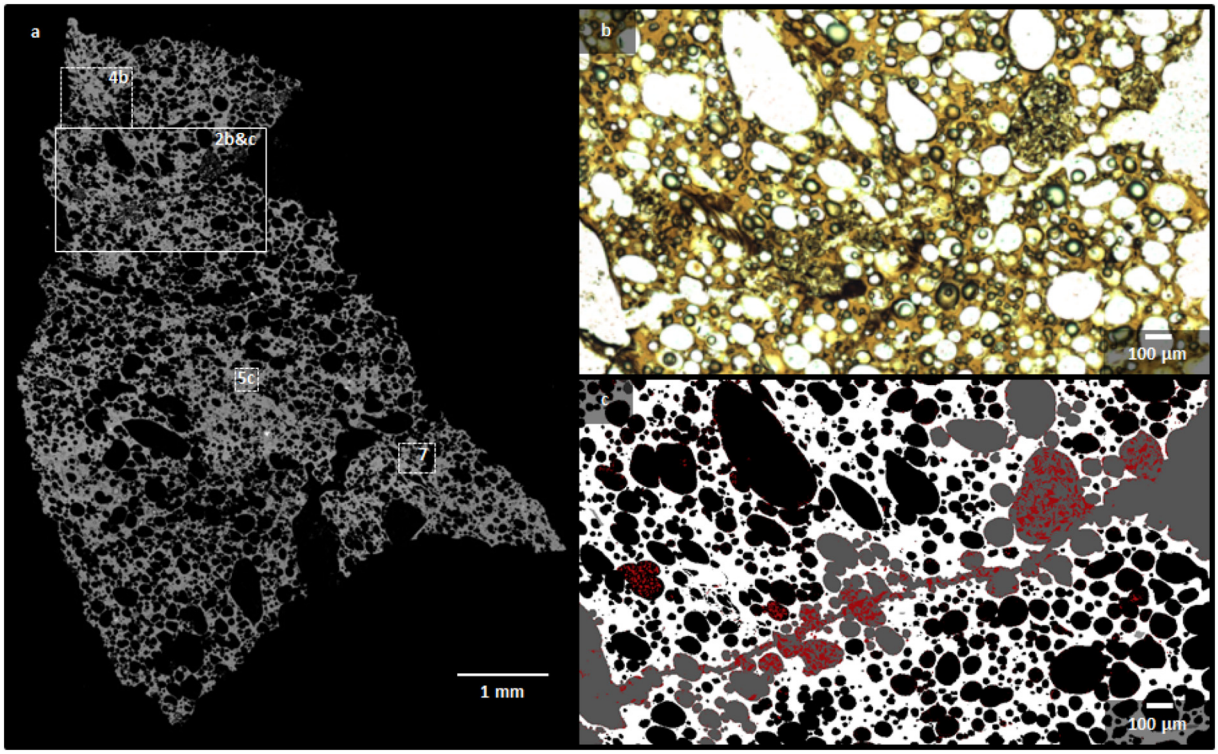

Fig. 2. Images showing an angular fracture containing ash particles within sideromelane. (a) A BSE mosaic image showing the whole clast - jökulhlaup sample Mul 6 unit 3a-1 8000–16000 2a (~5 × 8 mm). Rectangles with solid lines highlight the area shown in parts b and c, whilst the dashed line rectangles outline areas shown in Figs. 4b, 5c and 7. Fig. 8 features within the area shown by Fig. 5c but is too small to depict here; (b) Photomicrograph in ppl detailing the fracture; (c) Simplified BSE image showing the same area as b, where bubbles have been coloured black, glass white, the background (and bubbles connected to the background) grey, and ash particles in red. (For interpretation of the references to colour in this figure legend, the reader is referred to the web version of this article.)

3.3. Infilled bubbles

Interconnected bubble networks also frequently contain particles (Figs. 5b, 6). As with the fracture-filling particles, these are predominantly angular, but include a significant proportion that are well rounded and sintered onto bubble walls (Fig. 7).

A compositional map was acquired within an irregular, highly deformed particle-filled bubble, which appears to form part of a series of interconnected bubbles (Fig. 5b). The particles are very small (≪63 μm), generally angular and crudely sorted, with linear bands of finer grains in the bubble centre and larger particles on either side. The orientation of this band matches the orientation of the main axis of the bubble. The surrounding tachylite matrix consists of Ca-rich (green) and Fe- and K-rich (pink) microlites, which are most likely plagioclase, diopsidic pyroxene and Fe/Ti oxides (±orthopyroxene) typical of mafic magmas and Katla basalts (Lacasse et al., 2007; Budd et al., 2016). This phase assemblage contrasts with particles inside the bubble, which are predominantly either K-rich (blue) lithics, more likely belonging to a more evolved melt, or sideromelane (grey) juvenile glass particles. There are only two significant places where the particles match their host composition and their geometry suggests they are fragments of broken bubble wall and therefore are most likely a product of sample preparation (as labelled in Fig. 5b). The foreign nature and the apparent sorting and imbrication of the remaining particles leads us to believe this is a magmatic feature.

3.4. High density microlite chains

The last compositional map (Fig. 5c) focused on an area containing abundant microlite chains within sideromelane. The microlite chains seem to connect crudely oval vesicles (Figs. 5c, 8), some of which appear partially collapsed (Fig. 8b). Many of the bubbles are surrounded by microlites (Fig. 8b). Various Fe-rich (red) and K-rich (blue) phases coincide with the location of microlite chains (Fig. 5c). These phases have both angular (Fig. 8a) and rounded (Fig. 8b) forms, suggesting that they are variably relaxed particles of a fragmented melt. The Fe-rich fragments (Fig. 5c) are either Fe-sulphides or Fe-Ti oxides. The K-rich fragments (Fig. 5c) are likely feldspar (both alkali and plagioclase) and silicic glass. EPMA analyses on select K-rich fragments reveal compositions consistent with dacite and plagioclase feldspar (see Section 3.8). K-rich particles within all the Fig. 5 maps are therefore interpreted to be fragments of silicic glass and/or crystal fragments derived from a more evolved melt. In contrast, the lower left hand region in Fig. 5c is almost devoid of both microlite chains as well as Fe/K-rich particles and appears more vesicular with relatively large, near spherical bubbles.

3.5. Other sintered textures

Sintering can be at times so extensive that it is unclear whether the original void was a bubble or a fracture (Figs. 9, 10). In total, of the basaltic clasts for which there are BSE images, 12 of the 15 jökulhlaup clasts and 8 of the 9 air-fall clasts, show evidence of particle sintering.

3.6. Geothermometry

Fe-Ti oxides yield an average temperature of $T = 1045 \pm 31$ °C (n = 45 pairs) for K1918 basalts (Fig. 11).

3.7. FTIR

One air-fall clast was analysed with FTIR and found to have a glass H_2O content of 0.08 wt% (Table 1), consistent with degassing to atmospheric conditions (e.g. Tuffen and Castro, 2009). K1918 jökulhlaup clasts have glass H_2O contents of 0.15–0.31 wt% (Table 1), consistent with a pressure elevated beyond atmospheric, but not equivalent to

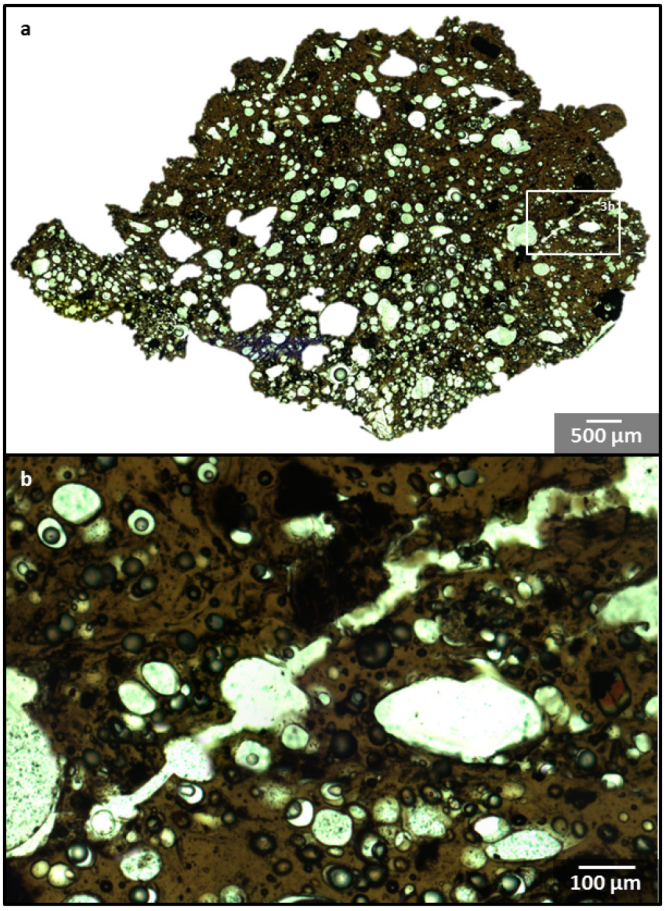

Fig. 3. Photomicrographs in ppl showing a rounded fracture within sideromelane, which contains ash particles near the clast margin. (a) mosaic overview of the whole clast – jökulhlaup sample Mul 6 unit 4–1 8000–16000 4a (~6 × 9 mm); (b) detail of the fracture, showing a transition from angular (left) to rounded (right) as it approaches the clast margin (far right). The rounded part of the fracture contains ash particles.

the full weight of the glacier. Using the pressure-solubility model VolatileCalc (Newman and Lowenstern, 2002) and assuming a Si-content of 47 wt% (consistent with Óladóttir et al. (2008)), 0 ppm of CO_2 (as measured) and a temperature of 1045 °C (estimated using geothermometry; Section 3.6), the jökulhlaup clasts likely quenched at pressures of 0.29–1.11 MPa. The loading pressure (P in Pa) can be estimated by multiplying gravity (g; 9.81 m s^{-2}) by the density (ρ in kg m^{-3}) and thickness of the load (h in m).

$$P = \rho g h \quad (2)$$

Thus a 400 m thick glacier (as was inferred to be the ice thickness over the vent in 1918 CE; (Sturkell et al., 2010)), with a density of 917 kg m^{-3} (Tuffen et al., 2010) would exert a pressure of 3.6 MPa, which is significantly greater than our estimates of quenching pressure for the jökulhlaup clasts. There is no systematic variation in H_2O content within the stratigraphic section sampled in Fig. 1c. Therefore taking the average jökulhlaup glass H_2O content (0.22 wt%), we can estimate that the average load during quenching was 0.59 MPa. This equates to approximately 65 m of ice, 60 m of water, 20 m of solid rock or 40 m of 50% vesicular basalt, assuming densities of 917, 1000 and 2770 kg m^{-3} for ice, water and K1918 basalt respectively, with errors of ~20%. However, natural samples often experience loading by a combination of materials (Tuffen et al., 2010; Owen et al., 2012; Owen et al., 2013b; Owen, 2016; Owen et al., in press).

3.8. Geochemistry

There is strong consistency between the EPMA data gathered at the University of Hawaii, that gathered at the University of Edinburgh and that already published for Katla (Fig. 12). EPMA data (Fig. 12) shows a bimodal distribution with sideromelane and tachylite clasts having ~47 wt% SiO_2 consistent with K1918 data published by Óladóttir et al. (2008), although the tachylite data is more scattered, likely due to these clasts being more microlite-rich (e.g. Fig. 4). In addition to the brown (sideromelane) and black (tachylite) clasts, most samples had a small percentage of clear/pale clasts with a trachyte/trachydacite to rhyolite composition similar to older silicic Katla eruptions (Lacasse et al., 1995; Newton, 1999; Larsen et al., 2001; Lacasse et al., 2007; Óladóttir et al., 2008). Sintered sideromelane particles have similar compositions to the larger discrete sideromelane clasts (Fig. 12). Sintered K-rich particles found within an area of extensive microlite chains within a sideromelane clast (Fig. 5c) were found to have compositions consistent with plagioclase feldspar and dacite (Table 2). Although a relatively high Fe content (potentially from crystal contamination) meant they were excluded form Fig. 12, they are also consistent with the published data from older silicic Katla eruptions.

4. Discussion

4.1. Evidence of gas and ash transport within permeable pathways

Many of the samples contain fractures and/or have connected bubbles, some of which contain small particles of fragmented material. It is possible for such features to form during poor sample preparation. Grinding during thin section making may fracture the rock, break thin bubble walls connecting vesicles and produce small particles which may then lodge in void spaces. It is also possible for fractures to form during quenching. However, both cooling-contraction cracks and sample preparation cracks should be angular as they happen <Tg, whereas most of our observed fractures show rounded morphologies that indicate a degree of viscous deformation and relaxation (Figs. 3b, 4, 5a), suggesting they experienced temperatures >Tg. Also, we would expect particles distributed during sample preparation to be random. However, what we have observed in the K1918 deposits is a very organised distribution of particles throughout the clasts.

Most of the particles are found in fractures and bubbles that are connected, and rarely within isolated bubbles (Figs. 2–6). When particles do occur in apparently isolated bubbles, they are often in close proximity to a bubble chain (e.g. Figs. 2c, 6a) and we suspect that they are actually connected in the third dimension. Fig. 9 shows clear areas of infilled bubbles and clear areas with none. These distribution patterns are hard to explain with poor sample preparation. Furthermore, the particle filled bubble in Fig. 5b seems to show layering parallel to the axial plane of the bubble, consistent with clastic deposition of particles within a stream of gas, as documented in silicic tuffisite veins where internal laminae are parallel to fracture walls (Tuffen et al., 2003).

Furthermore, compositional maps (Fig. 5) reveal that within both fractures (Fig. 5a) and bubbles (Fig. 5b) the phase assemblage and composition of the particles is at least partly distinct from that of the host, yet consistent with K1918 textures and geochemistry. All three compositional maps in Fig. 5 reveal silicic particles and felsic crystal fragments with compositions consistent with older silicic eruptions (Fig. 12). It is most likely that particles introduced through grinding in thin section preparation would be exclusive to the host. In Fig. 5b, there is almost a 100% inconsistency; there are only a few particles consistent with the composition and textures of the tachylite host, with the vast majority being particles of silicic and basaltic glass. We hypothesise that the tachylite particles do represent poor sample preparation, given their close proximity to the host and jigsaw-like fit,. However, the vast majority of the particles cannot be explained by this and we speculate that they are a primary feature, based on their foreign nature, and layering.

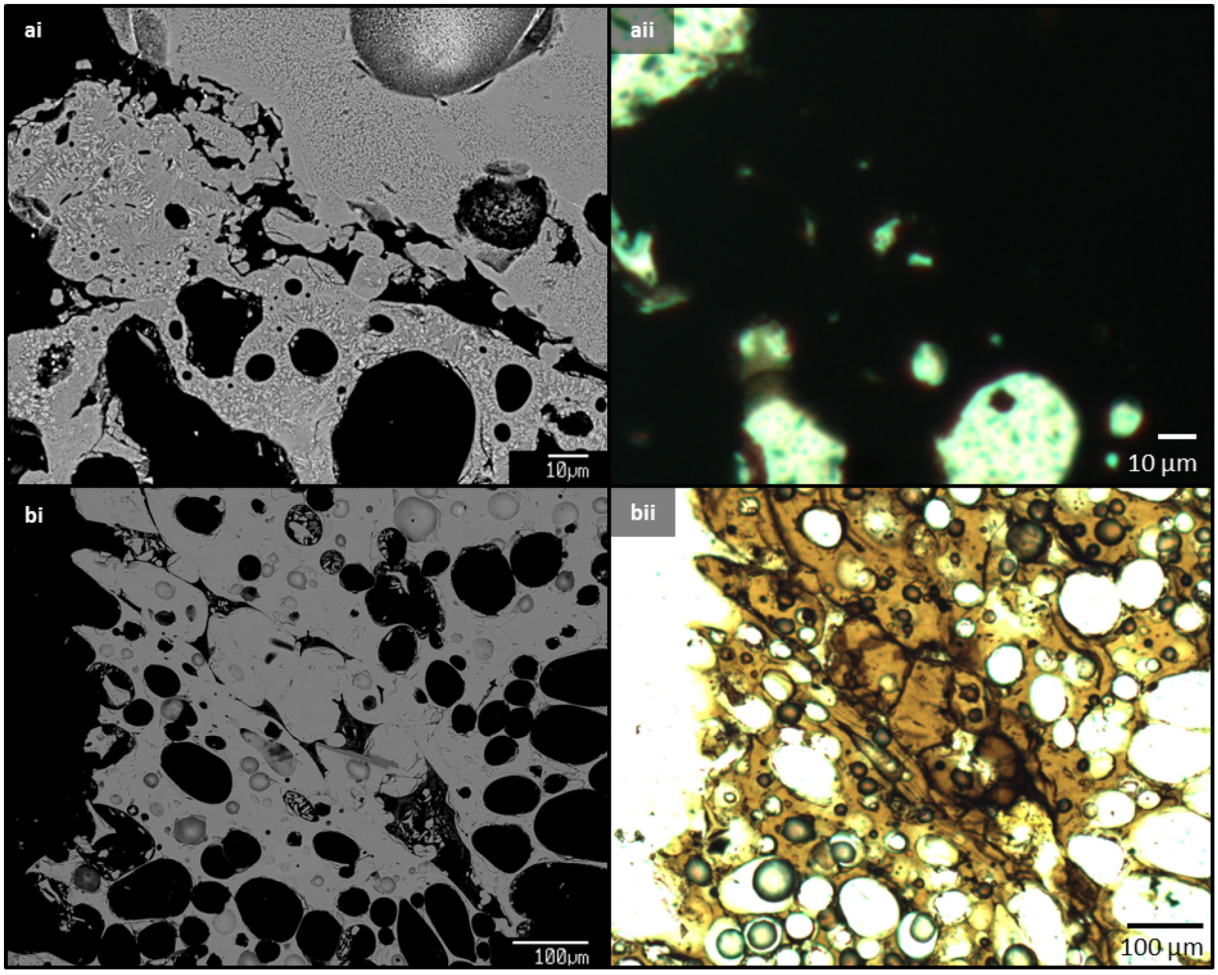

Fig. 4. Images of fractures containing partially sintered particles. The ash particles are connected to the host, and each other, via 'necks' of various sizes. The suffix refers to the image type, with (i) denoting BSE images and (ii) denoting thin section images taken in ppl. (a) A ~20 μm wide partially filled fracture within the tachylite part of a jökulhlaup clast - Mul 6 unit 4–1 8000–16000 3a (see Fig. 10a for context). Rounded tachylite ash particles have sintered onto the fracture wall with the boundary marked by a microlite chain; (b) A ~100 μm wide fracture that has almost healed within a sideromelane jökulhlaup clast - Mul 6 unit 3a-1 8000–16000 2a (see Fig. 2a for image location). The fracture is filled with rounded particles, which have sintered to each other and the fracture walls. The area immediately adjacent to the fracture is less vesicular than the surrounding melt.

The presence of sintered particles (Figs. 4, 5a, 7, 9, 10) further demonstrates that particle deposition was a *syn*-eruptive, high-temperature process as sintering indicates that some of the particles experienced temperatures >Tg within the fractures/connected bubbles. Some fractures and particle-particle contacts are almost fully healed (e.g. Fig. 4b), making it difficult to deduce the original fracture wall or particle boundary (e.g. Fig. 5a). Therefore, fractures may have been wider than currently observed. The presence of K-rich particles, collapsed vesicles and microlite chains in the host immediately surrounding the fracture in Fig. 5a further supports this notion. This thorough healing and compaction is analogous to that documented in welded rhyolitic tuffisites (e.g. Tuffen and Dingwell, 2005).

Furthermore, there are textures consistent with clast re-amalgamation; we interpret that Figs. 9 and 10 show former clasts embedded within larger clasts, with small particles sintered to the former clast walls and to each other, within boundary zones (Figs. 9d, 10f). This is germane to tuffisite vein interiors (Saubin et al., 2016) again suggesting initially larger permeable pathways than the preserved features.

Evidence for volatile transportation can be seen as local heterogeneity in bubble textures. Arguably, the vesicle-poor area neighbouring the fracture in Fig. 4b failed to vesiculate as much as the surrounding glass due to volatile depletion following diffusive loss into the degassing fracture (see Section 4.6). Similar textures have been observed in rhyolitic Chaitén bombs (Saubin et al., 2016; Webb et al., 2017).

We therefore hypothesise that bubbles (Figs. 5b, 7, 9) and fractures (Figs. 2, 3, 4, 5a) have acted as pathways for the transportation of both juvenile and lithic material, analogous to tuffisite veins in silicic pyroclastic material (Rust et al., 2004; Saubin et al., 2016). Systematic transport is shown by the organised distribution of particles and was likely facilitated by gas flow evidenced by diffusive loss shown by the apparent vesicularity gradient surrounding the fracture in Fig. 4b. Relaxed fracture morphologies and sintering suggest that both the fractures and particles within them experienced temperatures > Tg and thus we believe it to be a syn-eruptive process that occurred within the conduit.

4.2. Evidence of former gas and ash transport within healed permeable pathways

Partially collapsed vesicles surround many of the features of interest, e.g. the fracture in Fig. 5a, the vesicles containing sintered particles in Fig. 7, the area of intense microlite chains and Si-rich particles in Fig. 8 and the sintered particles in Fig. 10c. These collapsed vesicles always transition into microlite chains (Figs. 5a, 7, 8b and 10c). Furthermore, the bubbles in Fig. 8b are surrounded by microlites. Thus, we believe some of the microlite chains represent healed vesicles.

Microlite chains also appear to have formed between sintered particles (e.g. Figs. 4ai and 10g). Arguably, the similarity in size and morphology of the microlite chains in Fig. 5a to the intra-fracture particles could

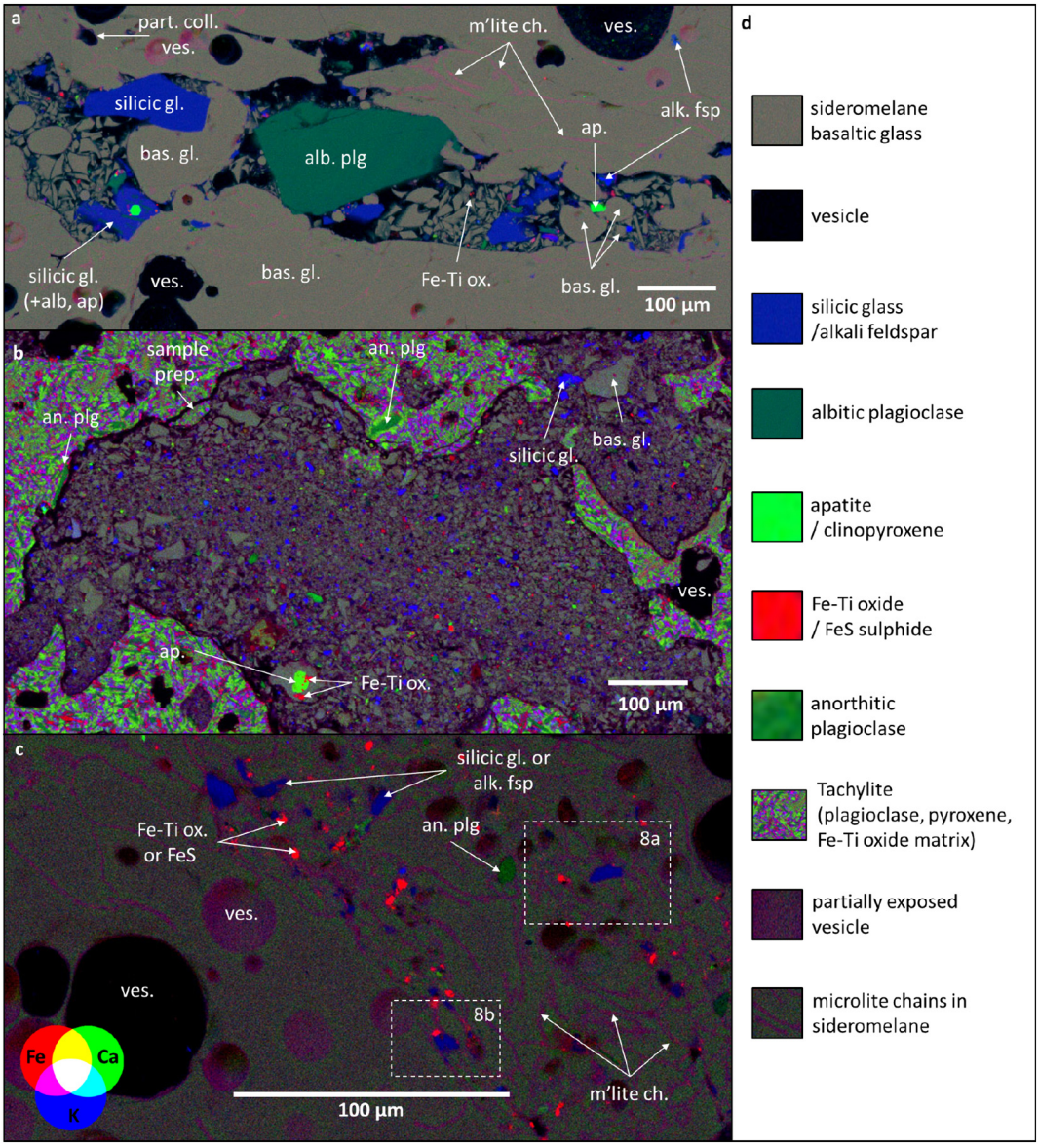

Fig. 5. Compositional maps showing a particle-filled fracture (a), a particle-filled bubble (b), and an area of extensive particle-bearing microlite chains (c). Colours represent relative element abundances according to the legend in the bottom left corner (Fe-rich = red, Ca-rich = green, K-rich = blue, Fe and Ca -rich = yellow, Ca and K –rich = turquoise, K and Fe –rich = pink and areas rich in Fe, Ca and K = white). (d) Offers an interpretative summary. (a) A ~200 µm wide particle filled fracture within a sideromelane jökulhlaup clast - Mul 6 unit 3a-1 2000–4000 3a. The particles are both basaltic sideromelane and fragments from a more evolved melt, and have both sub-angular and rounded morphologies. Microlite chains are present in the surrounding basaltic glass. See Fig. 16 for fracture location and ppl/BSE images; (b) A particle-filled irregularly shaped bubble which appears to be connected to other particle-filled bubbles (e.g. upper right). The host is microlite-rich tachylite from an air-fall clast - Sol 3E 8000–16000 3a, but the particles are predominantly sideromelane basalt and K-rich particles from a more evolved melt. These particles are highly angular and small, and show slight near-horizontal lineation with larger particles being near the upper and lower bubble walls. There is clear sample preparation damage to the upper bubble wall as labelled; (c) An area of extensive microlite chains within a sideromelane clast from jökulhlaup sample Mul 6 unit 3a-1 8000–16000 2a (see Fig. 2a for context). The microlites (pink) occupy the upper right part of the image and coincide with small fragments of various compositions. The lower left part of the image is void of microlites and particles but contains near-spherical bubbles. The dashed line rectangles outline areas shown in Fig. 8a and b. (For interpretation of the references to colour in this figure legend, the reader is referred to the web version of this article.)

mean that they represent the boundaries of former particles that have since sintered and compacted into the surrounding host.

Whether microlite chains represent collapsed vesicles (e.g. Fig. 8b) or the margins of former particles (e.g. Fig. 10g), they represent healed void-spaces. This is further evidenced by the relatively high S content (Fig. A1) of the microlite chains surrounding the fracture shown in Fig. 5a. Furthermore, it suggests that these facilitated volatile transport with vapour-phase precipitation occurring on former fracture/bubble/clast walls. In fact, in compositional maps, the microlite chains often appear similar in colour to partially exposed bubbles (Fig. 5). The coincidence of these microlite chains with silicic particles (e.g. Figs. 5c, 8) suggests that these healed voids also transported particles. Thus, we believe the dense area of microlite chains and foreign particles in Fig. 5c represents a healed transport pathway for a particle-rich fluid phase.

There is an apparent compositional similarity between the matrix delineated by these microlite chains and the surrounding microlite-free host basalt glass (Fig. 5c). However, the compositional maps shown in Fig. 5a and b indicate that basaltic fragments make up the majority of fragmented particles. Therefore, it is likely that the permeable pathways that carried the K-rich particles in Fig. 5c also transported basaltic particles. Evidence for this comes from the fragment of anorthitic plagioclase in Fig. 5c; an An-rich plagioclase likely has a mafic source. Apart from the mineral fragment, the basalt is now indistinguishable from the host and therefore likely juvenile in origin. This suggests that Fig. 5c represents a juvenile magma that fragmented (along with a

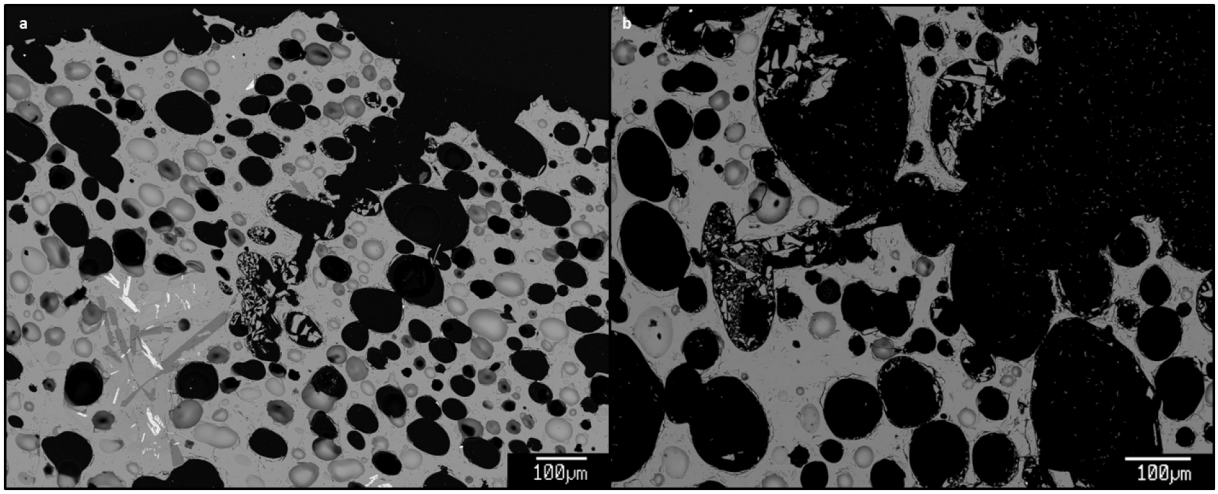

Fig. 6. BSE images showing examples (a and b) of particle-rich bubble chains in sideromelane jökulhlaup clasts. In both examples, the bubble chain appears to widen as it approaches the clast margin (upper right corner), however, the particles are most abundant at the opposite end. Particles are predominantly absent from nearby isolated bubbles. (a) is from Mul 6 unit 2–1 8000–16000 2a and (b) is from Mul 6 unit 3a-1 8000–16000 3a.

minor percentage of felsic origin) and was then transported in a permeable pathway, which then collapsed and healed. Small vesicles then grew in the scarred remains (Fig. 8).

Microlite chains also often surround fractures/permeable pathways (Figs. 5a, 10) indicating that they may have partially healed. However, in Fig. 5a, there are K-rich particles embedded into the basaltic glass even beyond the zone of microlite chains surrounding the particle-filled fracture. This is evidence of near complete healing. The apparent progressive welding around Fig. 5a suggests that the fractures were once considerably wider than they appear in some of the images; this healing of pathways is akin to tuffisite veins (Tuffen et al., 2003).

4.3. Origin of the basaltic particles

Most of the bubble- and fracture- filling particles have compositions consistent with K1918 basalt (Figs. 5 and 12), suggesting that it is juvenile material. This suggests that at least two fragmentation events were involved in the production of the K1918 clasts: firstly to produce the small particles, which are now trapped in the clasts, and lastly to produce and expel the clasts that were sampled. Sintering and healing is apparent between these two events and it is possible that there were further fragmentation events, however the rapid sintering rates of basalt makes it difficult to deduce how many fragmentation events occurred in total.

The fact that the first fragmentation event did not expel the particles suggests that it may have happened within the conduit, but at shallow level owing to the low H_2O contents (Table 1), low vesicularities of the particles (Figs. 2–10) and incomplete sintering (Figs. 2–10), suggestive of short residence times (see below).

Some clasts also show evidence of incomplete fragmentation (fracturing without significant displacement or expulsion) and brittle deformation (Fig. 13). The fragments of glass between the fractures share similar sizes, morphologies and vesicle textures to the fracture and bubble filling particles seen throughout the samples (e.g. Figs. 5, 6). This sample therefore represents an inefficient fragmentation event that failed to expel particles. It is likely linked with one of the early fragmentation events that produced fragments of glass that then infiltrated the remaining melt through connected bubbles and fractures.

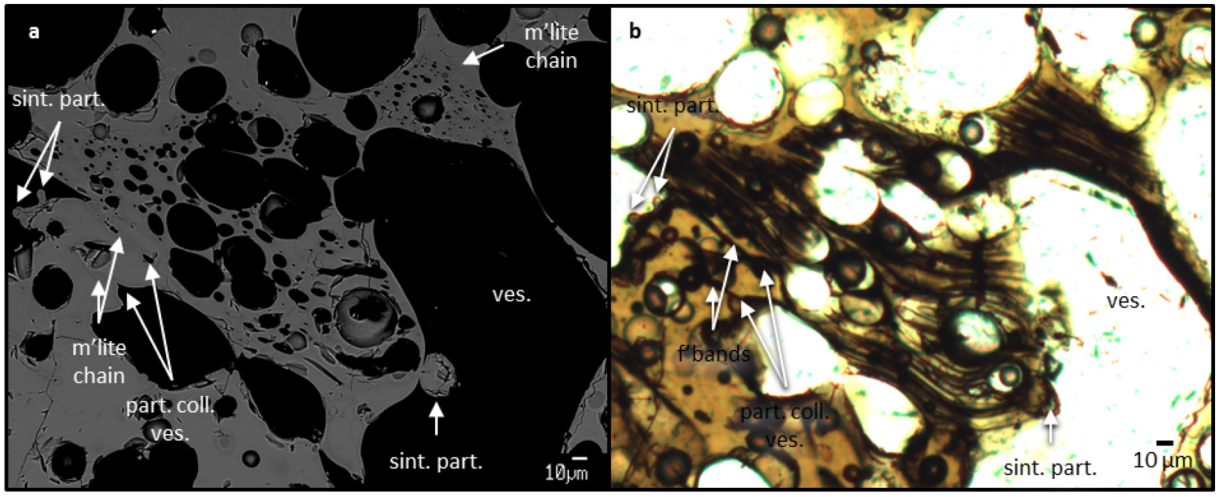

Fig. 7. Images (a: BSE; b: ppl) showing sintered particles within bubbles in a sideromelane jökulhlaup sample - Mul 6 3a-2 8000–16000 2a (see Fig. 2a for context). A round particle (~20 μm) is sintered to the wall of a large bubble (right side of the image), with a microlite chain marking the boundary. On the far left of the image is the edge of a bubble with two smaller sintered particles adhered to the bubble wall. The centre of the image is occupied by an area with a high number density of small bubbles, which appears flow banded in part (b) and is outlined by a microlite chain. In the neighbouring glass beneath, there are partially collapsed vesicles, clearly visible in part (a), which pinch out into additional microlite chains; these also appear as flow bands in part (b).

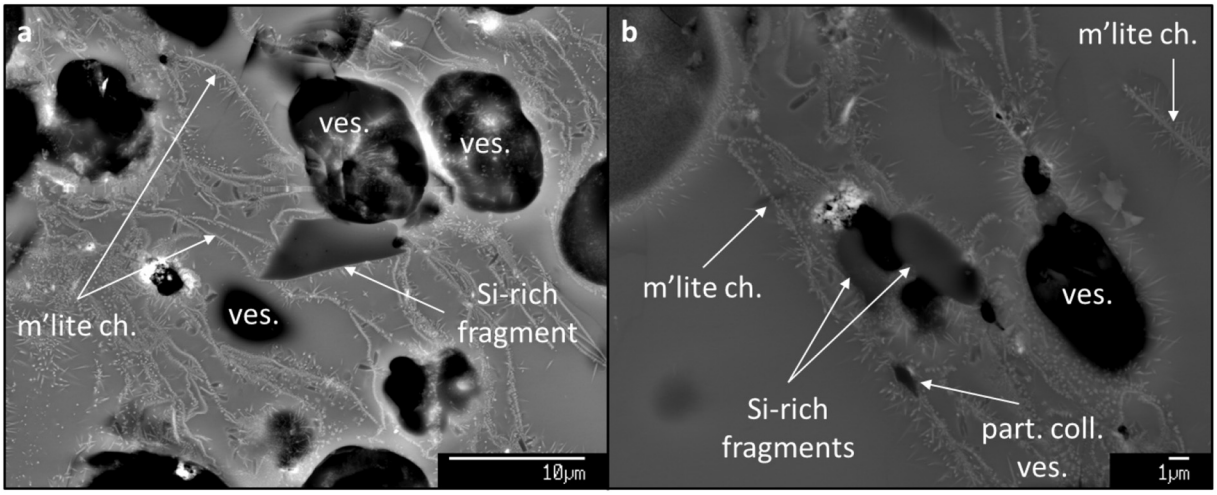

Fig. 8. Images showing dark grey fragments of Si-rich material (revealed to be dacite and plagioclase feldspar through EPMA spot analyses; see Section 3.8) within a basaltic glass (pale grey) riddled with microlite chains (white lines) and small bubbles (black), some of which appear partially collapsed. This area has also been mapped compositionally (Fig. 5c) and the whole clast (jökulhlaup sample Mul 6 unit 3a-1 8000–16000 2a) can be seen in Fig. 2a. The Si-rich material appears in both angular (a) and rounded (b) forms.

4.4. Origin of the felsic particles

Although the majority of particles are basaltic, every compositional map (Fig. 5) revealed the presence of some K-rich particles that spot analyses showed to be fragments of feldspar and dacite (Table 2). Clear/pale clasts were also found to have compositions of a more evolved melt, consistent with older silicic Katla eruptions (Fig. 12) (Lacasse et al., 1995; Newton, 1999; Larsen et al., 2001; Lacasse et al., 2007; Óladóttir et al., 2008). In fact, there are extensive silicic outcrops within the Katla caldera, including some close (<4 km) to the inferred

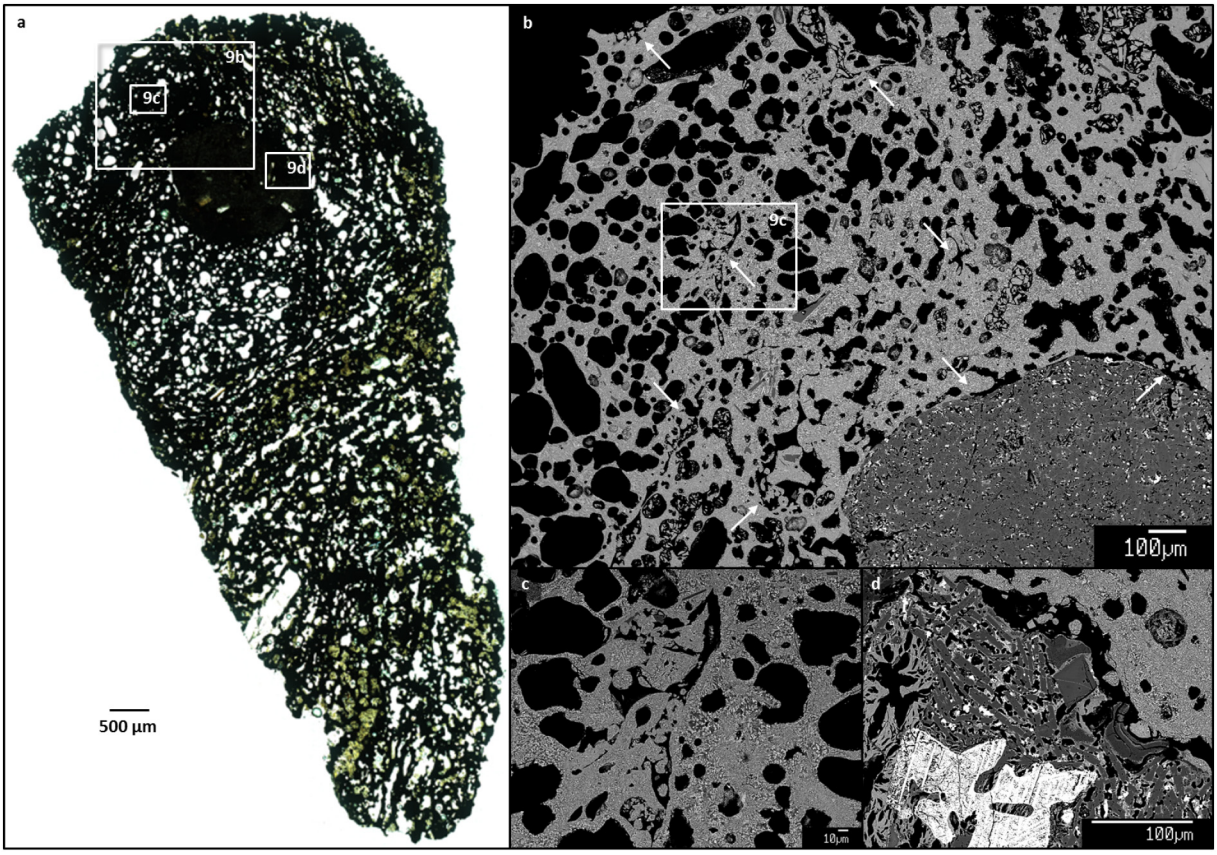

Fig. 9. Images (in ppl (a) and BSE (b-d)) showing sintered particles within void spaces. The rectangles indicate areas detailed in other parts of this image as labelled. (a) Mosaic overview of the whole clast, which is a tachylite jökulhlaup sample - Mul 6 unit 4–1 8000–16000 2a (~5 × 11 mm). There is a ~2 mm sized dark lithic in the upper part of the image and abundant particle filled bubbles, which appear pale brown in this image and appear to occupy distinct areas; (b) An overview of the upper part of the clast, with the lithic appearing dark grey in the bottom right hand corner. Bubbles (black) are nearly spherical on the left, but are significantly more irregular in the centre of the image. Irregular void spaces often coincide with sintered particles; particularly sintered areas are indicated with arrows; (c) An example of one of the highly sintered areas in part (b). The void in the image centre contains a large number of rounded particles; some of which are partially sintered onto the walls and others becoming indistinguishable from the matrix; (d) The boundary between the host clast (pale grey, upper right) and the lithic (dark grey) which contains a highly distorted phenocryst (white). There is a ~20 μm wide void space between the two, enclosing rounded particles of tachylite that are locally sintered onto the host clast. (For interpretation of the references to colour in this figure legend, the reader is referred to the web version of this article.)

1918 CE vent (Jóhannesson and Sæmundsson, 2014). We therefore hypothesise that the glassy K-rich particles represent fragments of evolved country rock (dacite, trachyte/trachydacite and rhyolite) that were mobilised during fragmentation and incorporated into connected fracture-bubble networks by a mobile fluid phase during ascent. This possibility was recognised by Budd et al. (2016) who used mineral-

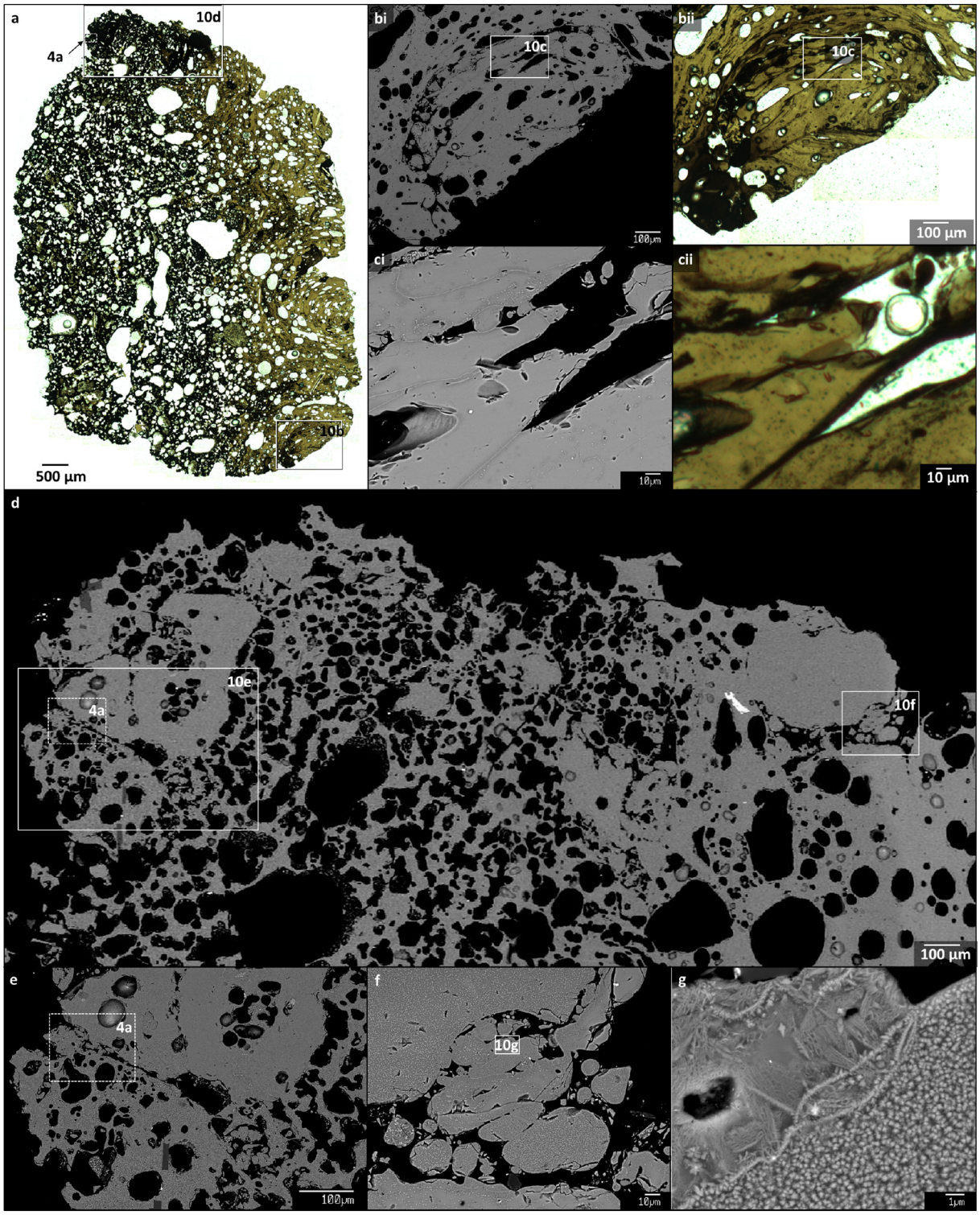

Fig. 10. Examples of sintering within the jökulhlaup clast Mul 6 unit 4–1 8000–16000 3a. (a) Photomicrograph mosaic image in ppl showing an overview of the whole clast (~6 × 9 mm), which is mixed tachylite (left) and sideromelane (right). Solid and dashed line rectangles express the areas shown in other parts of this figure and other figures, respectively, as labelled; (b) a semi-circular feature with a high abundance of rounded tachylite and sideromelane particles. It is unclear whether this was once a fracture which has welded shut or whether the whole area shows variably sintered clasts (i: BSE; ii: ppl); (c): detail of the area outlined in part (b) showing partially collapsed bubbles that contain rounded, sintered particles with microlite chains extending from the pinched point of each vesicle. (i: BSE; ii: ppl); Parts d-g show BSE images of the upper part of the clast; (d) overview mosaic image. The area shows extensive but heterogeneously distributed sintering. Arguably the large dense areas in the upper left and right-hand corners could represent former large particles spanning several hundred microns in diameter that have fused with the host. (e) and (f) illustrate the potential lower boundaries of these larger former particles, with small sintered particles prominent in this void space. The dashed rectangle in part e outlines the 'fracture' shown in Fig. 4a. (g) Detail showing the sintering interface between two rounded particles of tachylite, which is marked by a microlite chain of oxides.

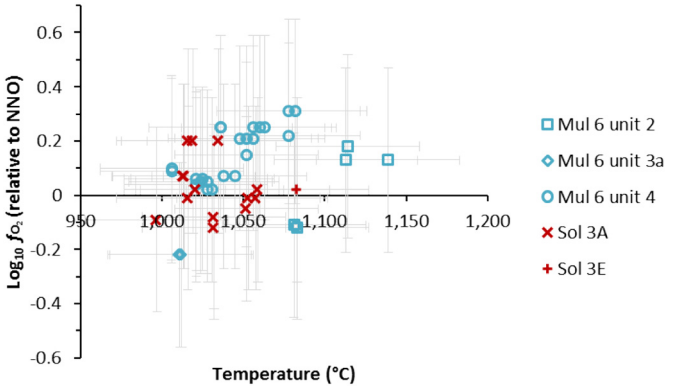

Fig. 11. Magma temperatures plotted against oxygen fugacity, estimated from magnetite and ilmenite compositions using the model of Ghiorso and Evans (2008). NNO refers to a nickel-nickel oxide oxygen buffer. Jökulhlaup and air-fall samples are prefixed by "Mul" and "Sol" and are coloured blue and red respectively. The error bars represent average absolute deviation (44 °C and 0.34 log units for temperature and oxygen fugacity (fO_2) respectively), calculated by Blundy and Cashman (2008) for the Ghiorso and Evans (2008) model. (For interpretation of the references to colour in this figure legend, the reader is referred to the web version of this article.)

melt equilibrium cystallisation pressures to infer multiple magma storage regions at Katla with the potential for new rising magma to intersect evolved magma within shallow storage regions.

4.5. Particle morphology, sintering timescales, and link with composition

The morphology of the silicic particles is generally angular, in contrast to the basaltic particles, which are more often rounded (Fig. 5a). Within magmatic fractures that have largely healed, the angular morphology of glassy silicic lithics (Figs. 5c, 8a) is surprising, as surface tension-driven shape relaxation would occur rapidly at basaltic eruptive temperatures.

We consider two possible explanations for why the silicic particles are generally less deformed than basaltic ones (Fig. 5a). Firstly, even though the Si-rich material was considerably hotter than its usual eruptive temperature, it would still have had a significantly higher viscosity than the basalt (Fig. 14) and therefore the timescales for deformation, shape relaxation and sintering would have been considerably longer (Vasseur et al., 2013). Secondly, being part of the country rock, the silicic material was likely incorporated at far lower temperatures than the juvenile basalt (1045 °C), and would thus have needed to first rise to temperatures >Tg in order to deform, further hindering sintering.

To investigate these two scenarios, and to produce some crude estimates of heating, relaxing and sintering timescales, we performed some basic first-order estimations (Appendix 2). The results show that owing to the small particle size, all of the intra-void particles shown in this study (typically ≪ 100 μm) would have likely reached thermal equilibrium within milliseconds (Fig. A4). The time taken to heat silicic particles (of this size) to basaltic magmatic temperature therefore seems insignificant.

Our inferred rounding/sintering timescales are only slightly longer (fractions of seconds) than timescales for thermal equilibrium, but are strongly viscosity-dependent (Vasseur et al., 2013). We therefore conclude that the rounding/sintering rate is the main process that controlled particle shape. Even at 1045 °C, which is significantly higher than its usual eruptive temperature, the viscosity of the silicic magma will be high enough to extend the rounding/sintering timescale by one or two orders of magnitude compared to basalt (Fig. A5). Consequently, for particles of comparable size, the basaltic particles can thoroughly sinter and heal before the silicic particles have relaxed to a rounded shape. These viscosity-controlled differences in rounding/sintering rate can therefore explain the angularity of silicic particles within a healed matrix of basalt in Fig. 5c, and the apparent deformation of a basaltic particle around a similarly sized angular silicic particle in Fig. 5a.

Estimating exact sintering times is difficult since timescales are extremely sensitive to composition, H_2O content and particle size (Fig. A5). These parameters will also be changing throughout the process, and it is difficult to deduce the original starting conditions from what is preserved in the samples (Pope, 2015).

Nevertheless, our simple calculations (Appendix 2) suggest that the sintering times, for the preserved particles within the fractures/bubbles/voids, were at most a few seconds. Any longer would have likely resulted in complete healing. For angular clasts, this process would have been even quicker, and/or the particles were injected below Tg; either way suggests near instantaneous injection, fragmentation and quenching. The fact that some of the voids contain both angular and rounded particles of similar sizes (e.g. Fig. 5a) suggest that there was momentarily a stream (albeit very short-lived) of gas and ash with particles entering the space at slightly different times.

Final quenching was likely closely linked with fragmentation at Katla. Fragmentation may have even been triggered or enhanced by magma-meltwater interaction. Even if not phreatomagmatic, there would have been abundant ice and meltwater in close proximity to the vent. FTIR analyses reveal that the jökulhlaup samples quenched under pressures consistent with loading from ice or water (see Section 3.7). The glassy nature of the sideromelane also implies rapid quenching.

It should be noted that the inferred residence time of variably sintered particles is not necessarily an indicator of the full duration of void opening. These voids, when first opened, may have been vapour- rather than particle-filled. Additionally, small (<100 μm) basaltic particles will fully sinter very rapidly (in fractions of seconds; Fig. A5), after which it will be difficult to recognise the former presence of particles. Some fractures are neighboured by K-rich fragments, collapsed vesicles and microlite chains that form crude particle-shaped patterns (Fig. 5a). We hypothesise that these textures represent former particles that fully annealed to the void walls, and that microlite chains often indicate former permeable pathways/healed voids (e.g. Figs. 5c, 8; see Section 4.2). However, it is difficult to determine the extent of healed pathways, because chemical diffusion and viscous flow will homogenise the sintered melt, ultimately leaving little/no trace of the former particle boundaries. For these reasons, we suggest that the voids were open over seconds, and only the final split seconds of the void life is preserved within our samples. We hypothesise that the preservation (particularly of angular particles) was possible due to rapid quenching in water, which must have occurred almost simultaneously with the final injection of particles. This indicates a very rapid succession of deformation that was brittle (to form the initial particles), ductile (to sinter the particles) and then brittle again (to expel and quench the particles).

Table 1
FTIR results showing glass H_2O contents for five K1918 clasts.

Environmental setting	Sample name	Mean H_2O content (wt%)	Standard deviation (wt%)	Number of successful analyses
Air-fall	Sol1A 8000–16000 4b	0.08	0.01	11
Jökulhlaup	Mul6 unit 2–1 8000–16000 2b	0.22	0.02	9
Jökulhlaup	Mul6 unit 2–1 8000–16000 4b	0.21	/	1
Jökulhlaup	Mul6 unit 4–1 8000–16000 1b	0.31	0.04	2
Jökulhlaup	Mul6 unit 4–1 8000–16000 4b	0.15	0.05	2

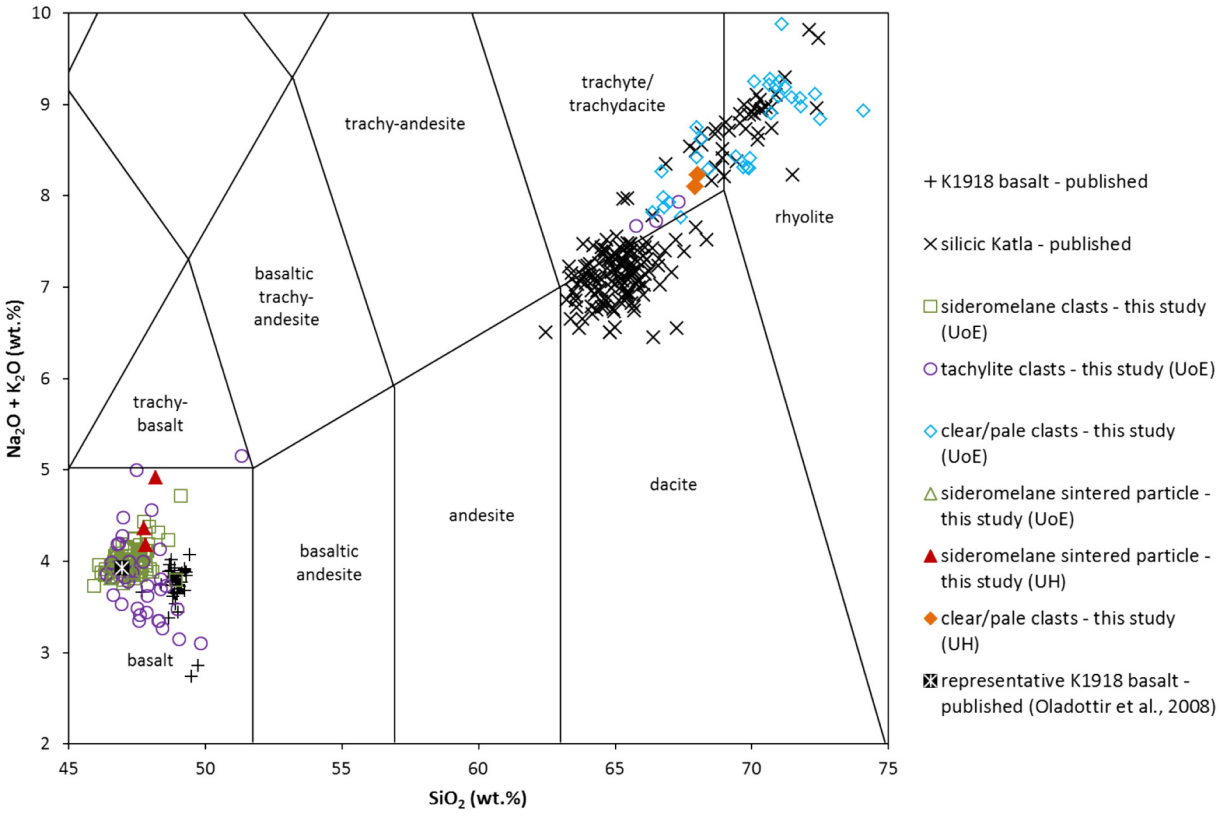

Fig. 12. A TAS plot of EPMA glass data from Katla showing published values (black) from K1918 and older silicic eruptions, as well as data from this study (colour). Clast types have been distinguished by colour either as brown sideromelane, black tachylite or clear/pale lithics. UoE (open symbols) and UH (filled symbols) denote the University of Edinburgh and the University of Hawaii respectively, which is a reference to the institution where the analyses were performed. 'Sintered particles' refer to small sintered particles within larger 'clasts'. Published K1918 data is from Óladóttir et al. (2008) and Budd et al. (2016) with the former used to represent K1918 geochemistry for density and solubility-pressure estimations. Published data of older silicic eruptions is from Lacasse et al. (1995), Newton (1999), Larsen et al. (2001), Lacasse et al. (2007) and Óladóttir et al. (2008). (For interpretation of the references to colour in this figure legend, the reader is referred to the web version of this article.)

4.6. Diffusive loss of volatiles through fractures, and timescale for open system degassing

To further investigate the lifetime of the permeable networks we provide estimates of diffusion timescales (Appendix 3). There are several lines of evidence that permeable networks have facilitated diffusive loss of volatiles. Firstly, microlite chains and bubble walls are usually S-rich (Fig. A1). These microlite chains were likely former voids and particle boundaries (see Section 4.2), where S-rich gases circulated and deposited along the suture zones. Secondly, the glass surrounding some of the voids (e.g. Fig. 4b) is noticeably deficient in terms of bubble textures compared to the surrounding melt.

Bubble-poor, fracture-adjacent basaltic glass could indicate diffusive volatile loss into the void-space. If a low pressure void opens within magma, it will allow volatile escape, drawing H_2O out of the melt through diffusion. Subsequent decompression of the melt during ascent will then yield lower vesicularities than the surrounding melt that has not experienced diffusive loss (Saubin et al., 2016; Webb et al., 2017). Furthermore, the vesicularity and bubble size of particles within the Fig. 4b fracture are extremely similar to the glass adjacent to the fracture. This further supports the notion of diffusive loss and suggests that the glass within and immediately surrounding the fracture was able to diffuse to a similar H_2O concentration which was lower than the host melt, prior to the final vesiculation event.

Using 1D diffusion calculations to quantify the development of an 80 μm wide H_2O depleted zone (Appendix 3), we estimate that the fracture shown in Fig. 4b experienced volatile loss by diffusion towards the melt-fracture interface for ~40 s. This particular fracture has been extensively healed. We therefore infer that the pre-quenching lifetime of other less-sintered fractures (e.g. Figs. 4a, 5a, 10) was much shorter. Our diffusion timescales are therefore close to timescale estimates for sintering and residence times of intra-void particles discussed in the previous section. Nevertheless, there is clearly a range of sintering and quenching timescales preserved within those clasts, as expected in fragmented magma with a wide range of grainsizes and textures.

4.7. The nature of the void spaces

Small particles occupy many different void spaces e.g. angular fractures (Fig. 2), relaxed, more rounded fractures (Fig. 3), tuffisite vein-like features (Figs. 4, 5a), bubbles and bubble chains (Figs. 5b, 6, 7) and the boundary space between sintered clasts (Figs. 9, 10). At times,

Table 2
EPMA analyses of three particles within the area of extensive microlite chains in Fig. 5c (sample Mul 6 unit 3a-2 8000–16000 2a). The analyses are consistent with the compositions of dacite (top two) and plagioclase feldspar (third analysis).

Analysis number	SiO_2	TiO_2	Al_2O_3	FeO	MnO	MgO	CaO	Na_2O	K_2O	P_2O_5	Cl	TOTAL	Inferred material
1	63.76	1.85	13.45	7.39	0.16	1.31	4.19	2.09	2.31	0.21	0.08	96.79	Dacite
2	65.70	1.67	14.83	6.66	0.15	1.35	3.64	4.13	2.17	0.21	0.07	100.57	Dacite
3	54.45	0.33	28.60	1.40	0.00	0.29	11.33	4.99	0.23	0.00	0.00	101.63	Plagioclase feldspar

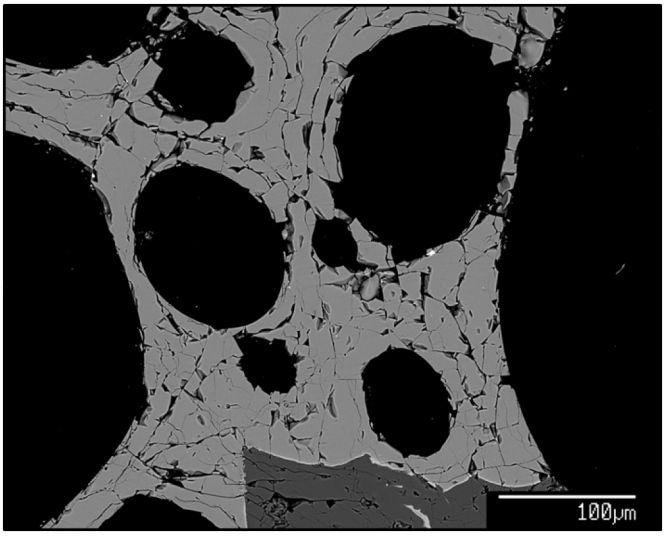

Fig. 13. A BSE image showing highly fractured sideromelane within jökulhlaup sample Mul 6 unit 4–1 8000–16000 1a, which could have acted as a source for small particles that later sintered with fractures and bubbles elsewhere (e.g. Figs. 5, 6). The dark grey shape at the bottom is a phenocryst.

the sintering is so extensive that it is difficult to deduce the original void shape (Fig. 9c). For instance, some features could be interpreted as a vein-like fracture (Fig. 4a) or a boundary zone between clasts

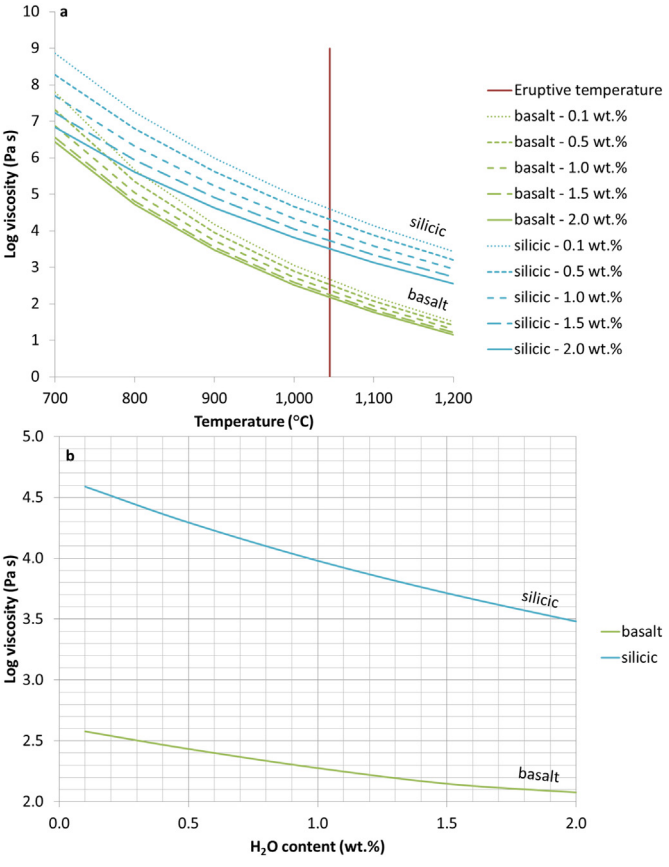

Fig. 14. viscosity as a function of composition, temperature and H_2O content, according to the viscosity model of Giordano et al. (2008). For the 'basalt' and 'silicic' composition the analyses that most closely resembles published data was used (Fig. 12). The red line depicts our inferred eruptive temperature (1045 °C). (a) viscosity plotted against temperature, for different compositions (colours) and H_2O contents (line styles); (b) viscosity plotted against H_2O concentration for our inferred eruptive temperature of 1045 °C. (For interpretation of the references to colour in this figure legend, the reader is referred to the web version of this article.)

(Fig. 10d, e). Nevertheless, there is textural and compositional evidence for gas and particle transfer in fractures, bubble chains and sintered breccias (often in the same clast; Figs. 2a, 10a), and in reality, all are likely to occur, as they do in rhyolitic magma (Stasiuk et al., 1996; Schipper et al., 2013).

We propose a hypothetical model where localised explosions fragment both the country rock and some of the juvenile material, which are jetted into fractures, vesicles and mobile breccias, either moments before or during ejection from the vent (Fig. 15).

4.8. Comparisons with rhyolite-hosted tuffisite veins

Tuffisite veins are the quenched remains of fractures that form in silicic melts and provide a pathway for gas and ash particle transport. As described in the previous section, it is unclear whether some of the K1918 textural features represent true 'veins', bubble chains or interclast spaces; we appear to have a spectrum of void spaces that include all end-members. Nevertheless, these samples clearly show evidence of permeable pathways for gas and ash particle transport, that heal shut with time in repeated fragmentation cycles (Fig. 15) analogous to tuffisite veins.

The circulation of gas through a permeable network is clear from S-rich microlite chains (Fig. A1) and gradients in bubble textures surrounding voids (Fig. 4b). The mobilisation of particles is demonstrated by the systematic distribution of particles within clasts (Figs. 2c, 6a, 9a) as well as bedding within bubbles (Fig. 5b), which was also reported in rhyolitic tuffisites from Torfajökull (Tuffen et al., 2003). Furthermore, foreign particles (silicic particles within basalt (Fig. 5a, b and c) and sideromelane particles within tachylite (Fig. 5b)) must have been transported to their current location. Transport clearly happened at magmatic temperatures because numerous particles show evidence of rounding/sintering, which is also a feature of rhyolitic tuffisites (Tuffen and Dingwell, 2005).

The intra-void particle size in the K1918 clasts (10–200 μm diameter) is similar to those found in tuffisite veins and, like rhyolitic tuffisites, angular fragments dominate over rounded ones (Tuffen et al., 2003; Tuffen and Dingwell, 2005). It is difficult to compare the size of the fractures themselves. In rhyolitic conduits, tuffisite veins can be millimetres to centimetres in width and are seen to extend over >5 m in dissected examples (Tuffen et al., 2003). Based on water concentration heterogeneities, veins are inferred to extend >100 m vertically (Saubin et al., 2016). The fractures we observed tended to be tens of μm in width (Figs. 4 and 5). We suspect that pathways were initially wider and have narrowed through welding processes (Section 4.2), but it is also worth noting that our observations were limited to small particles (<16 mm). This begs the question; were the permeable pathways in the K1918 basalt limited to a small size, or did significantly larger fractures exist, and have been destroyed by the explosive nature of this eruption? Indeed the sintered breccia in Fig. 10 could be evidence for a larger-scaled feature, as are the xenoliths trapped within clasts (e.g. Fig. 9). Perhaps the whole conduit was acting as a permeable pathway for fragmentation and sintering, allowing communication with the surrounding, damaged country rock.

However, there is one clear difference; the permeable pathways in the K1918 basalt seem to be much more transient than rhyolitic tuffisites. Estimates from simple thermal (Appendix 2) and diffusion rate calculations (Appendix 3) suggest that the K1918 fractures were open for just seconds before quenching, whereas inferred tuffisite vein lifetimes in rhyolite may span ~10^3–10^5 s (e.g. Castro et al., 2012). This difference can be explained by the lower melt viscosities and higher H_2O diffusivities that will occur in the hotter basaltic system. Interestingly, however, inferred diffusion distances are similar; typically tens to a few hundred μm (Castro et al., 2012; Berlo et al., 2013; Saubin et al., 2016).

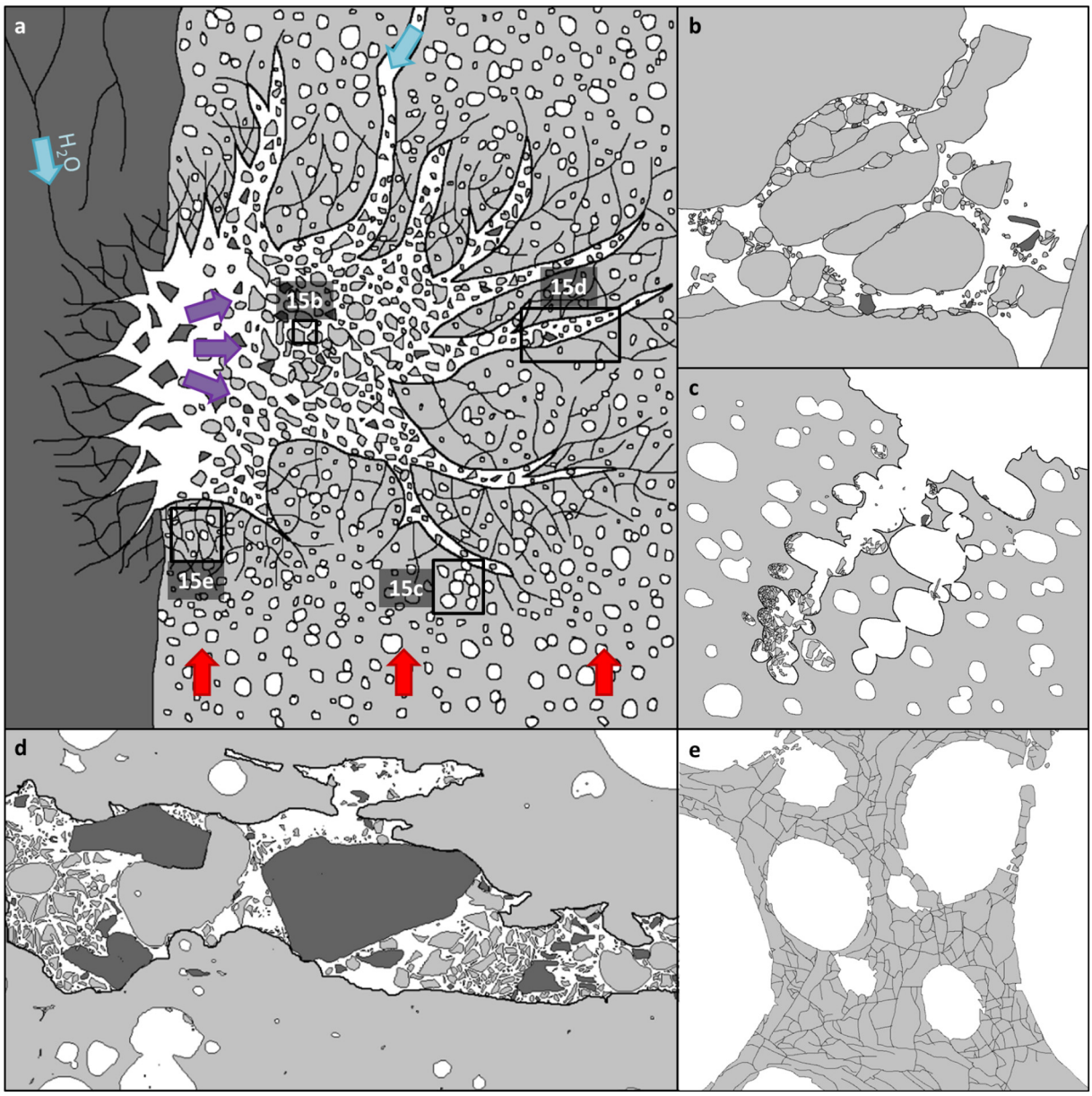

Fig. 15. Our interpretative model to explain the various textures seen within the K1918 clasts. In (a) a vesicular basaltic melt (pale grey) is rising next to older silicic country rock (dark grey) from past Katla eruptions. A localised explosion, either caused by magmatic fragmentation, or more likely phreatomagmatic fragmentation from H_2O percolating down through fractured country rock, shatters both the silicic country rock and the neighbouring basaltic melt. This creates a hot mobile phase of particles that begin to sinter together (b), infiltrate chains of connected bubbles (c) and infiltrate the transient fractures formed by the explosion (d). The melt surrounding the blast zone has been shattered (e) representing an incomplete version of the fragmentation within the blast zone. These features would have only existed for, at most, seconds before thorough welding took place. Preservation requires further fragmentation to expel and quench the clasts into a water-rich environment, which was perhaps facilitated by meltwater percolating down through cracks in the damaged magma and wall rock. Parts b, c, d and e represent Figs. 10f, 6a, 5a and 13 respectively.

4.9. Links with eruptive behaviour

In silicic systems, permeable pathways in magma (whether connected bubbles or tuffisite veins) often serve to enhance magma degassing and outgassing, and may contribute to a transition towards more effusive activity (Jaupart and Allègre, 1991; Jaupart, 1998). Permeable outgassing is also thought to occur during subglacial volcanism and contribute towards transitions in eruptive behaviour (Owen et al., 2013a; Owen et al., 2013b; Owen, 2016). Whilst the K1918 samples show plenty of visual evidence for permeable pathways (Figs. 2–10), evidence of an effusive phase is lacking from the 1918 CE Katla eruption, although deposits from such a phase could be obscured under the present glacier (Owen, 2016). Nevertheless, the clasts collected were small fragments from the large-volume jökulhlaup deposit that originated from explosive fragmentation. In rhyolitic melts, tuffisite veins *alone* are thought to be inefficient at degassing and outgassing magma, with spacing of <1 mm required to outgas the magma sufficiently to cause the transition to effusive behaviour (Castro et al., 2012). Therefore, it is possible that the magmatic fractures observed within the K1918 samples were simply insufficient to degas the magma efficiently. However, tuffisite veins that intersect permeable foams *are* considered a highly efficient mechanism of magma degassing, and may induce a transition to effusive behaviour, e.g. at Chaitén (Castro et al., 2012; Saubin et al., 2016). A large proportion of bubbles within the K1918 samples contain ash particles. Therefore, gas was presumably transported in connected bubbles as well as fractures (e.g. Fig. 6). If exsolved volatiles were able to efficiently outgas why was the eruptive style so explosive?

One explanation could be the extremely transient nature of the permeable pathways in the basalt. Simple calculations to estimate sintering (Appendix 2) and diffusion (Appendix 3) timescales suggest vein lifetimes of seconds or less, approximately five orders of magnitude shorter than in rhyolitic systems (Fig. A5) (Castro et al., 2012). However, diffusion in basalt would have also been fast, and our inferred diffusion profile is of similar length scale to those seen in rhyolite (Castro et al., 2012).

An alternative model is that the permeable pathways (fractures and connected bubbles), in the K1918 magma, potentially served as mechanisms for enhancing explosivity rather than to defuse the eruption. There are two explanations for this: (1) the pathways connected shallow magma to that of a deeper source, allowing gas to be transported up from depth and thus adding to, rather than reducing the volatile content of the fragmenting magma (Houghton and Gonnermann, 2008; Castro et al., 2012); (2) the pathways allowed meltwater (from the overlying melting glacier) to efficiently infiltrate into the magma column, facilitating fuel coolant interaction (FCI) and thus explosive fragmentation.

The former has been used to explain periods of heightened activity at Stromboli where open system degassing brings high levels of CO_2 from a deep magma source (Allard, 2010). However, if this was the case, one would expect volatiles to diffuse from the fracture into the melt and thus for the magma adjacent to fractures to be volatile-rich compared to the surrounding melt. We saw no evidence for this in our samples. In fact, if anything the opposite is true, as there is an apparent bubble-poor zone around the fracture in Fig. 4b.

It is more likely that the permeable pathways served to enhance fragmentation by meltwater infiltration from the overlying glacier, triggering FCIs. Abundant meltwater would have been present at the time of the eruption and there is evidence that the jökulhlaup samples quenched under loading from water/ice (Section 3.7). The microlite-poor nature of the glass also suggests rapid cooling. In this sense, the permeable fracture pathways in the basalt enabled pre-mixing of magma and external water, enhancing phreatomagmatic fragmentation, as inferred for rhyolitic magma (Austin-Erickson et al., 2008).

We therefore propose the following hypothesis to explain the sintered permeable pathways (Fig. 15): 1) rising vesicular magma melted overlying ice producing water; 2) As the magma neared the surface it began to fragment (Fig. 15a). It is difficult to underpin the initial cause of the fragmentation; some of the clasts are highly vesicular with high bubble number densities which could indicate magmatic fragmentation but there would have also been abundant meltwater which could have filtered down to the magma through cracks triggering phreatomagmatic fragmentation. Nevertheless, this fragmentation event did not expel the melt fragments but instead injected them (Fig. 15b) into connected bubbles (Fig. 15c) and fractures (Fig. 15d) in the remaining intact melt. The blast also fragmented country rock which also got incorporated into these permeable pathways; 3) the hot magma induced sintering of the particles and some of the pathways partially or fully healed; 4) only seconds (or fractions of seconds) later, a further explosive event expelled the now fully fragmented magma out of the vent into a watery environment inducing rapid quenching. The cause of this fragmentation event was likely meltwater infiltrating the now highly fragmented magma through the permeable pathways created by the first fragmentation event; 5) this explosion likely produced more small particles and opened further fractures, allowing more meltwater to infiltrate the conduit in a self-fuelling and repeating process with a cycle of seconds or less.

Repeating fragmentation events (Fig. 15) not only explain the particle filled void spaces but the apparent clasts welded within clasts (e.g. Fig. 9). Our model (Fig. 15) could also help to explain why the K1918 eruption was so powerful; magma-water mixing massively promotes fuel coolant interactions (Zimanowski et al., 1991; Morrissey et al., 2000), and meltwater ingressed within permeable pathways would have allowed plenty of opportunity for this. It could also explain why the glacier melted so quickly and produced such a powerful flood; if the under-side of the glacier is constantly being bombarded with a hot slurry of fine particles there will be both mechanical erosion as well as rapid thermal melting from the large-surface area to volume ratio.

Finally, our model (Fig. 15) may help to explain why the sintering textures have been preserved so well, particularly in the jökulhlaup clasts; abundant meltwater, perhaps also within the permeable pathways would promote rapid quenching. The jökulhlaup samples, unlike the air-fall samples, also show that they quenched under elevated pressure (Section 3.7), which could perhaps be explained by being emplaced into water, which would ensure the continued quenching of the particles and the best preservation of features. Note that although there is evidence of sintered particles within the air-fall samples, all of the best examples of particles sintered within permeable pathways were found in the jökulhlaup clasts.

4.10. The extent of the permeable network within Katla 1918 pyroclasts

Sintered particles perhaps present the best evidence for clast transportation around the glass transition and therefore the presence of a permeable network within the K1918 magma. Although sintering is present in 80% of the K1918 clasts examined, rounded particles only make up a very small percentage of the bubble and fracture-filling particles, which are predominantly angular (e.g. Figs. 5, 6). When particles are angular, infilling could be thought of as an artefact of poor thin section preparation (e.g. lack of sufficient ultrasonic cleaning to rid the sample surface of adhering ash). However, the layered structures and exotic compositions, in Fig. 5b, consistent with older silicic Katla magma (Fig. 12 and Section 4.2) emphatically indicate that these are primary textures. As the particles in Fig. 5b are almost exclusively angular, this conclusion can potentially be applied to all infilled bubbles and fractures (regardless of particle morphology) which are found in a significant proportion of all K1918 clasts (e.g. Fig. 9a).

Similarly, it is easy to quickly dismiss angular fractures as a feature formed through quenching or sample damage during thin section preparation. However, even the angular fractures contain particles favourably over nearby isolated bubbles (Figs. 2c, 3b, 6) suggestive of permeable pathways.

Thus we believe that the vast majority of the particles, fractures and connected bubbles seen in the K1918 pyroclasts to be primary features indicative of the transportation of small particles of juvenile and lithic material in a mobile fluid phase through a permeable network within the 1918 Katla magma.

4.11. How common are permeable gas and ash transporting pathways within basalt?

Although sintered particles within permeable pathways are common in rhyolite, they are thought to be exclusive to silicic eruptions, yet particle sintering was found in 80% of the basaltic K1918 clasts examined. There are three explanations for this absence from the literature: 1) the process that forms them is extremely rare but there were some conditions specific to the K1918 eruption that allowed them to be formed; 2) they are commonly created during basaltic eruptions but rarely preserved; near simultaneous fragmentation and quenching during K1918 allowed this; 3) they are common features, preserved readily in basaltic samples, but often overlooked, perhaps when observed, mistaken for bad sample preparation.

We favour the latter option, given the high abundance of sintered/transported particles and permeable pathways within our samples (Section 4.10). These features are difficult to detect in conventional forms of observation (e.g. Fig. 4), requiring high resolution analytical instruments (e.g. field-emission microprobes or SEMs) for imaging and compositional mapping. Most of the features were not obvious or else completely invisible in ppl (e.g. Fig. 4aii).

Angular bubble-occupying particles are fairly common in natural volcanic samples, as are flow bands. Careful image comparison has revealed that in the K1918 clasts, flow bands in ppl images tend to represent microlite chains in BSE images (Figs. 7, 10, 16), which in turn we infer to represent healed void-spaces (e.g. Figs. 5, 8, 10, 16). It therefore seems, at least in K1918 samples, that extensive flow banding represents (partially) healed fractures that may be filled with sintered particles (e.g. Fig. 16).

The features described in this paper are extremely widespread; evidence of particle sintering was present in most clasts, with particularly good examples of fracture and bubble-filled particles present in jökulhlaup samples. It would be useful to know whether such ash filled magmatic fractures and bubbles exist in other basaltic eruptive products; and if so whether they are exclusive to subglacial or subaqueous environments. Are they features that are actually common and have simply been overlooked, being attributed to bad sample preparation or interpreted as flow banding? Or are they actually a rare feature, uniquely preserved by the K1918 eruption?

5. Conclusions

We use textures and compositions to infer that fractures and connected bubbles acted as pathways for transport of gas and ash within basaltic melt during the Katla 1918 eruption. Evidence appears primarily in the form of angular to healed fractures, sintered ash particles, differing compositions between the ash particles and host, apparent sorting of particles, S precipitation and a zone of low vesicularity surrounding a partially healed fracture. Silicic particles and mineral fragments that belong to a more evolved melt indicate that material was incorporated from the country rock, and that both juvenile and lithic particles were transported through these systems, some of which have partly healed.

There are some similarities between these observed features and rhyolitic tuffisite veins. However, the basaltic pathways appear considerably smaller and more transient suggesting extremely rapid, near simultaneous and successive episodes of brittle-ductile-brittle deformation. These observations are significant, since it was previously thought that magmatic fractures and permeable gas/ash networks only formed in high viscosity melts. The presence of such features at Katla could be explained by rapid quenching, which has allowed the preservation of such features.

This discovery challenges our conceptions of magma degassing, fluid and particle transport, and the rheological properties of basaltic magma. In rhyolitic melts, tuffisite veins can cause a transition to more effusive activity. The fractures within the Katla basalt do not appear to have significantly degassed the magma as the clasts are still highly vesicular and erupted explosively. An alternative explanation is that the fractures served to enhance explosivity by providing pathways by which meltwater could infiltrate, enhancing both quenching and phreatomagmatic fragmentation. The discovery of these fractures therefore could have important implications for our understanding of the way in which basalt fragments.

We propose similar textures could be widespread in basaltic tephras from other settings but have been largely ignored to date as dismissed as sample preparation artefacts. However, these textures likely record key phases of magma damage, recycling and preparation for fuel-coolant interactions.

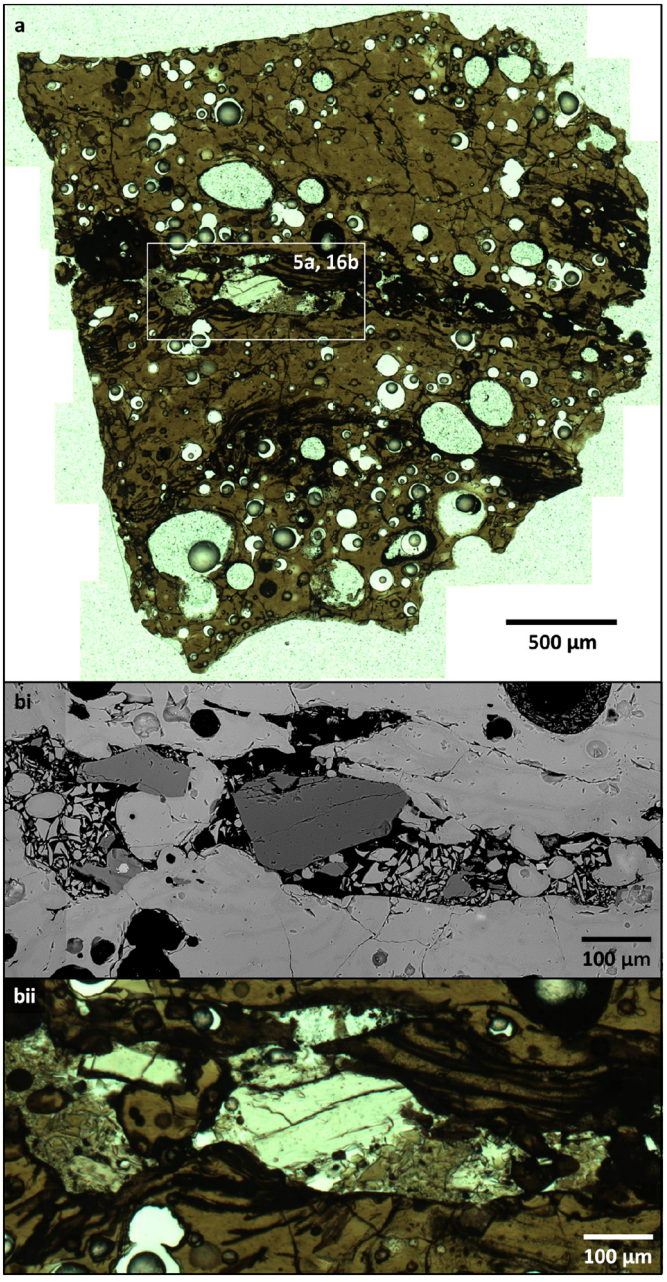

Fig. 16. A clast bearing a particle-filled sintered fracture that is inconspicuous in ppl, instead appearing as an area of intensive flow banding. (a) A ppl overview of jökulhlaup clast Mul 6 unit 3a-1 2000–4000 3a (~3 × 3 mm). The clast is predominantly sideromelane but has two dark horizontal stripes of intensive flow banding dissecting the sample; (b) Detail of the topmost dark stripe (see Fig. 5a for a compositional map of the same area); (bi) a BSE image showing a partially healed fracture full of sintered particles, surrounded by microlite chains; (bii) a ppl image of the same area showing flow bands around a feature that is much less obviously a particle filled sintered fracture.

Acknowledgements

Jacqueline Owen is the beneficiary of a post-doctoral grant from the AXA Research Fund. Thomas Shea and Hugh Tuffen were supported by a National Science Foundation grant EAR 1250366 and a Royal Society University Research Fellowship respectively. Chris Hayward and Debbie Hurst assisted greatly in lab analysis. Robert Duller, Lionel Wilson and Margherita Polacci contributed to fascinating discussions as did a great number of people from the University of Iceland, including Magnús Guðmundsson and William Moreland. We are grateful for the thoughtful and thorough edits provided by Jérémie Vasseur and an anonymous reviewer. Final thanks go to James Gardner for professional editing and insightful comments.

Appendix 1. Compositional maps

As described in the methods, EPMA was used to make compositional (x-ray distribution) maps. Five spectrometers were used to measure the relative abundance of S, Ca, Fe, K and either Na or F. The data was used to make single 2D intensity matrices as shown in Figs. A1, A2 and A3. These images were then combined to create the RGB composite image shown in Fig. 5. The relative abundance of all five elements was considered when making compositional interpretations as described in the text.

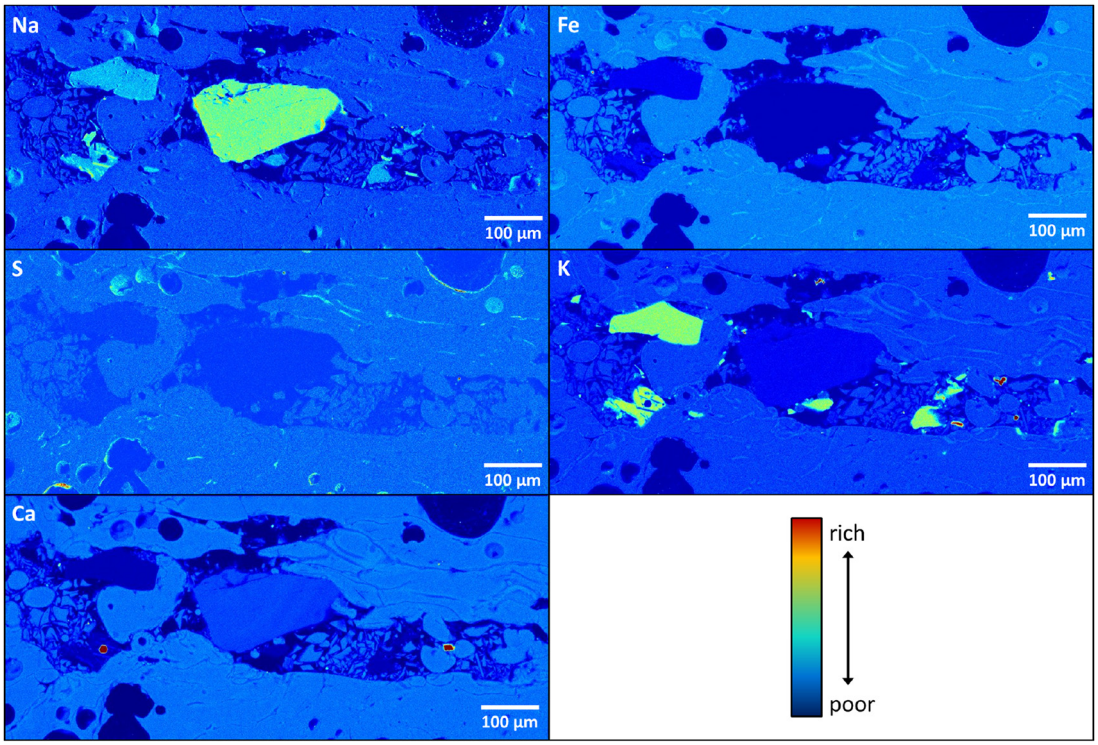

Fig. A1. 2D single intensity matrices for the fracture shown in Fig. 5a. Each image represents the relative abundance of a single element (Na, Fe, S, K or Ca) as indicated by the chemical symbol in the top left corner of each image. Hot and cold colours represent high and low abundances respectively.

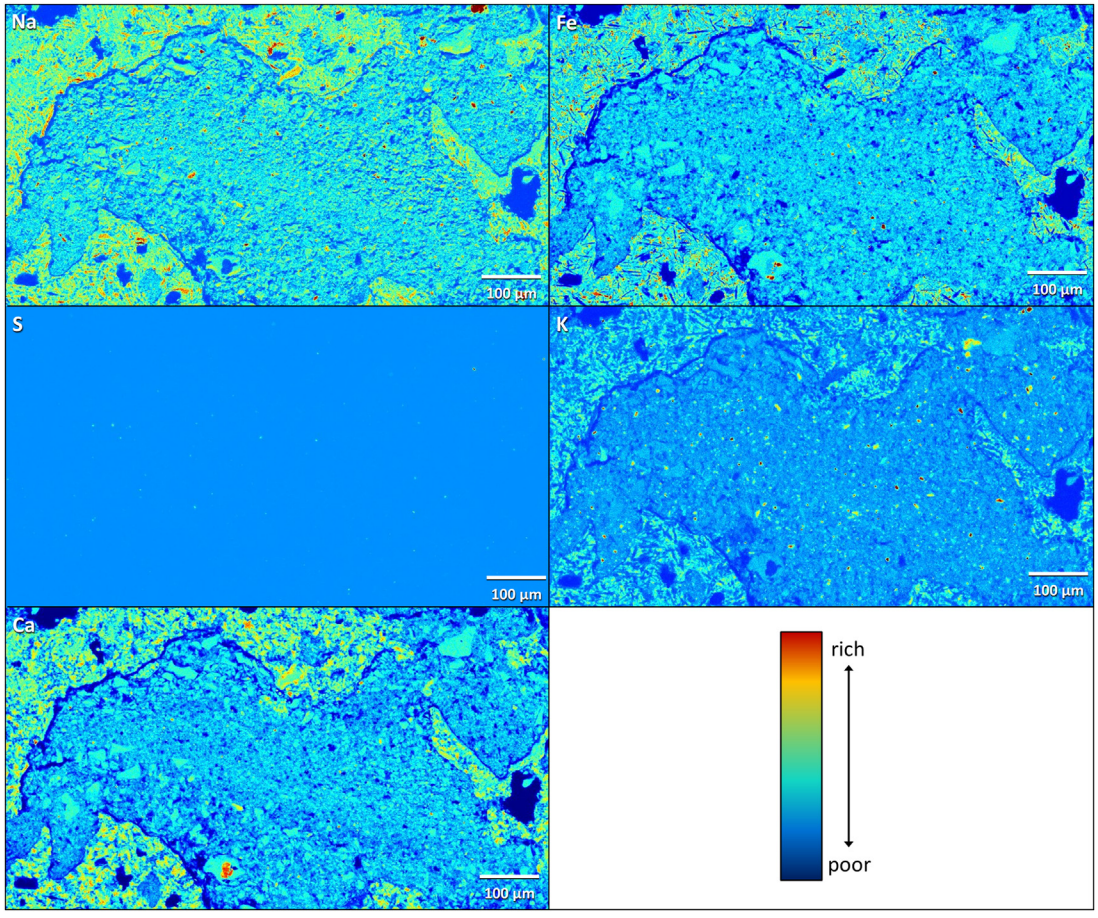

Fig. A2. 2D single intensity matrices for the particle filled bubble shown in Fig. 5b. Each image represents the relative abundance of a single element (Na, Fe, S, K or Ca) as indicated by the chemical symbol in the top left corner of each image. Cold and hot colours represent low and high abundances respectively.

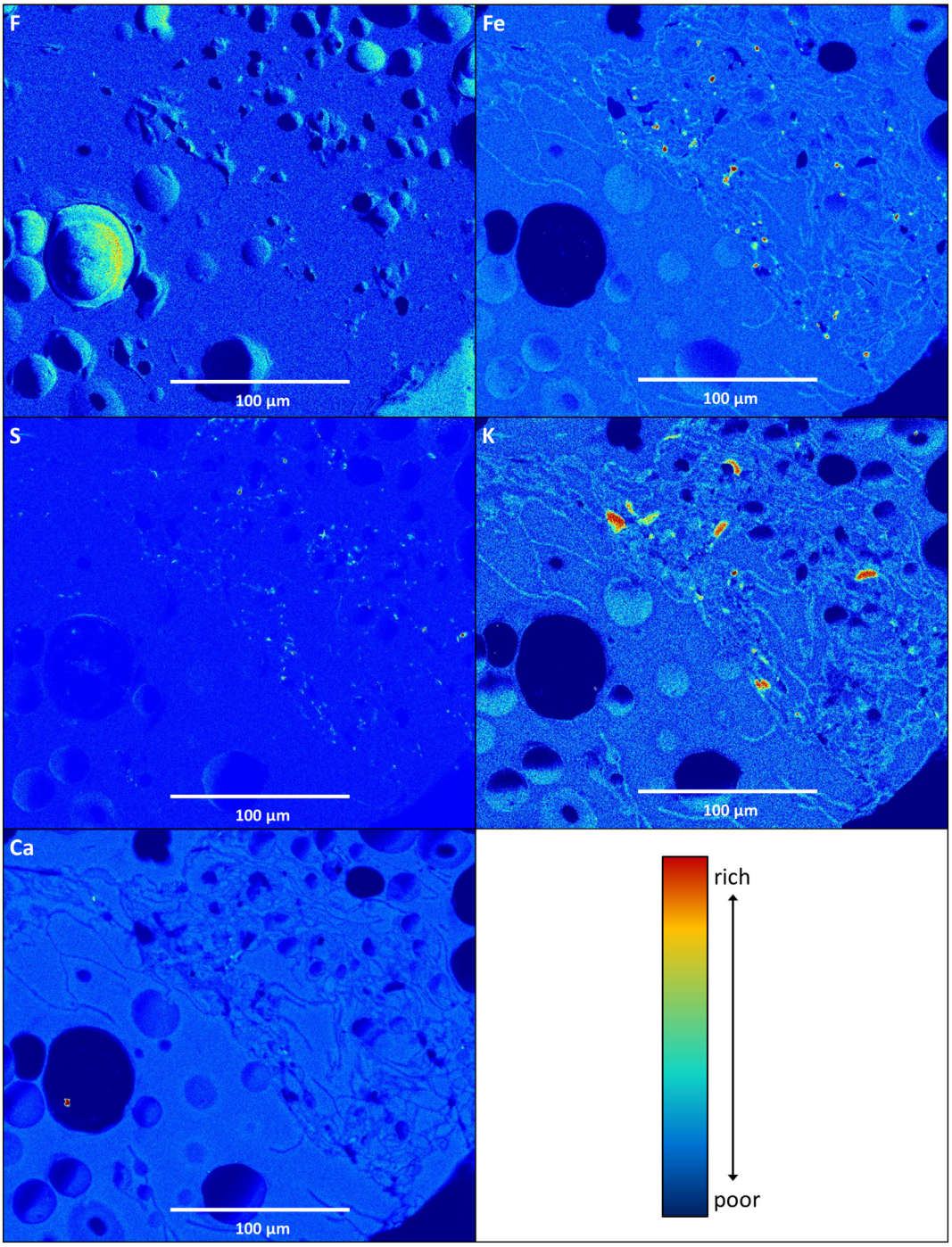

Fig. A3. 2D single intensity matrices for the area of intensive microlite chains shown in Fig. 5c. Each image represents the relative abundance of a single element (F, Fe, S, K or Ca) as indicated by the chemical symbol in the top left corner of each image. Cold and hot colours represent low and high abundances respectively.

Appendix 2. Thermal calculations to estimate sintering timescales

To estimate sintering timescales we assume a three step process: (1) thermal equilibration, (2) clast rounding, (3) welding to 'healed' state.

The fact that so many of the particles are angular suggests brittle fragmentation and therefore that the magma was below Tg. Furthermore, we hypothesise that the more evolved particles represent older silicic Katla material, which was incorporated into permeable pathways during magma accent, and therefore presumably entered the system at temperatures closer to ambient. Therefore, for these particles to sinter, the first step will be for them to gain magmatic temperature i.e. reach thermal equilibrium. The timescale for thermal equilibrium to be reached (t_{eq} in s) can be estimated using this equation (Wilson and Mouginis-Mark, 2003)

$$t_{eq} \sim \frac{r^2}{k} \tag{3}$$

where r is particle radius (in m) and κ is thermal diffusivity (in $m^2\ s^{-1}$). Thermal diffusivity varies ($0.5–2.0 \times 10^{-6}\ m^2\ s^{-1}$) as a function of temperature and to a lesser effect composition (Vosteen and Schellschmidt, 2003; Whittington et al., 2009; Eppelbaum et al., 2014), however, in the interests of simplicity we will take an ~average value of $1 \times 10^{-6}\ m^2\ s^{-1}$

which is considered the general thermal diffusivity for all silicates (Wilson and Mouginis-Mark, 2003).

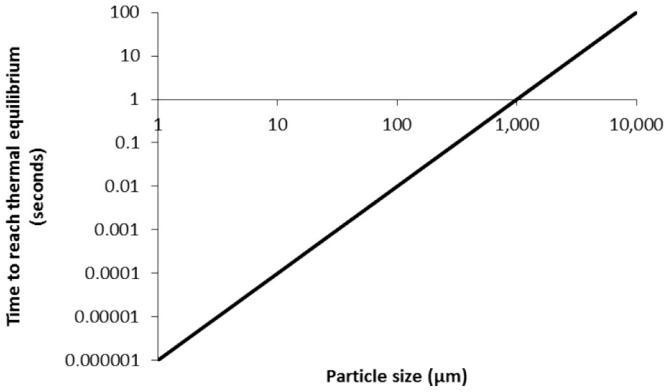

Fig. A4. Expected times for particles to meet thermal equilibrium as a function of particle size.

Typical intra-void particles are <100 μm and therefore would have reached thermal equilibrium in a matter of milliseconds (Fig. A4). We therefore, deem this process insignificant in effecting the timescale of sintering.

Many papers discuss the timescales of sintering e.g. (e.g. Uhlmann et al., 1975; Ristić and Milosević, 2006; Pope, 2015), however, these models assume that the starting media consists of spherical particles. Natural ash particles are not spherical. It seems from our samples that some of the ash particles have experienced rounding, whereas others have not, therefore, it would be interesting to estimate the timescale of this rounding/relaxation process that occurs prior to sintering. We are only aware of one study (Pope, 2015) that has tried to estimate rounding rates of natural samples however, this was performed on rhyolitic particles from Cordón-Caulle, Chile, and no general relationships were observed between rounding rate, grain size and temperature. We therefore turned to the equation used to estimate the rounding rate of vesicles within magma (Gardner et al., 2017):

$$\lambda = \frac{\eta r}{\sigma} \tag{4}$$

where λ is the relaxation time (in s) that a non-spherical bubble will take to relax into a spherical form, η is melt viscosity (in Pa s), r is particle radius (in m) and σ is melt surface tension (in N m^{-1}). When this equation was applied to the parameters of the particles used by Pope (2015) the calculated relaxation time was very similar to the timescales of clast rounding observed in their experiments. Therefore, we will use Eq. (4) as a proxy for the relaxation/rounding rate of Katla clasts.

Viscosities were estimated using the model of Giordano et al. (2008), our EPMA data and the assumption that the magma was 1045 °C. We also modelled typical rhyolite from Chaitén at 800 °C (Castro and Dingwell, 2009), where tuffisite veins and sintering are common (Castro et al., 2012; Berlo et al., 2013; Saubin et al., 2016). Although surface tension (σ) varies as a function of various magmatic parameters (Bagdassarov et al., 2000; Mangan and Sisson, 2005; Gardner and Ketcham, 2011; Gardner et al., 2013), H_2O content is the only parameter considered to have a significant effect, with melt composition and temperature only playing a very minor role (Walker and Mullins, 1981; Bagdassarov et al., 2000; Gardner et al., 2013; Gardner et al., 2017). We therefore chose a single value of 0.3 N m^{-1} for all modelling which is consistent with literature values for relatively dry silicate melts (Taniguchi, 1988; Phillips et al., 1995; Gardner and Denis, 2004; Sumner et al., 2005).

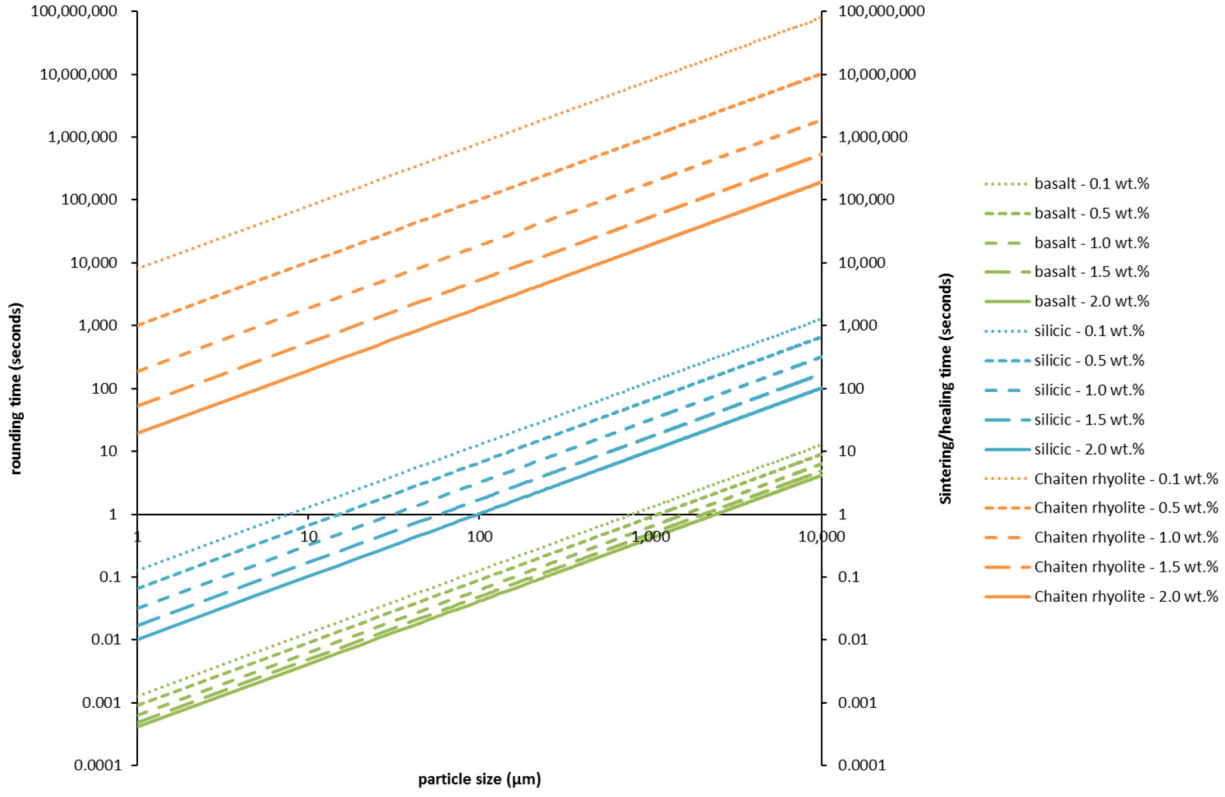

Fig. A5. expected times for particles to round/sinter as a function of particle size and dissolved H_2O content (0.1–2.0 wt% as shown in the legend). Note that the rounding timescale and sinetering/healing timescale were calculated in the same way and therefore have the same value. Therefore, the combined rounding and sintering rate can be found by simply doubling the values in this figure. Green and blue lines refer to samples within this study at an assumed temperature of 1045 °C. The orange lines model Chaitén rhyolite at 800 °C (using composition data from Castro and Dingwell (2009)) where tuffisite veins are often found.

Once connections are made between particles, the pore spaces can 'heal' through viscous flow (Ristić and Milosević, 2006; Vasseur et al., 2013). The following equation can be used to estimate the timescale τ_s of viscous sintering (Vasseur et al., 2013)

$$\tau_s = \frac{R_i \eta}{\gamma} \quad (5)$$

where R_i is the initial radius, η is melt viscosity and γ is the melt-vapour interfacial tension. Note that this is essentially the same equation as that for the viscous relaxation of bubbles (Vasseur et al., 2013). As we are using the latter to estimate the rounding rate of the particles, and because we disregard the timescales for thermal equilibrium as being insignificantly small, then our combined timescale for the complete sintering of the sub millimetric 1918 CE Katla particles to become healed glass can be estimated by doubling Eqs. (4) or (5) and thus the values in Fig. A5.

Typically, intra-void particles are approximately ≤100 μm in diameter. For basaltic particles with 0.2–0.3 wt% H_2O (as measured with FTIR) this equates to rounding times of ≤0.1 s, and thus full healing times of approximately ≤0.2 s. These resultant times, are perhaps a little unrealistically short. However, they give an idea of relative differences between particles e.g. it can be seen that silicic particles of the same size will take considerably longer to sinter (Figs. A5, A6). Furthermore, even if the absolute values were out by a few orders of magnitude (it is difficult to suggest reasons for errors larger than this), then it still equates to extremely short residence times for the permeable networks and times much shorter than for Chaitén rhyolite at 800 °C (Fig. A5) (Castro et al., 2012) where our estimated values closely match observations (Pope, 2015). Thus we can be confident that our estimates are reasonable ball park amounts.

The thermal estimations can help explain some of the particle morphologies as well as shed insights into timescales. For example, our calculations suggest the large rounded basaltic particle in Fig. A6, had to be hot for at least 0.13 s to be deformable, however if it had been at 1045 °C for >0.26 s it would have compleletely annealed with the surrounding melt. The angular silicic particle (blue) next to it required ~8 s at 1045 °C to relax into a sphere. The fact that it has not rounded, therefore suggests a residence time < 8 s. The smaller rounded basaltic particles require residence times of 0.05–0.1 s, whilst the angular clasts must have been resident for <0.05 s. If we assume that the microlite chains (in pink above the fracture) represent the former bounderies of annealed particles then using their approximate dimensions, these particles must have been present for more than >0.14 s to anneal together. All of this is consistent with a fracture opening for a fraction of a second, and having a momentary stream of particles before quenching. However, it is impossible to tell the extent of the annealed particles bejond the pink microlites (presumably prolonged heating will completely homogenise the melt), therefore a more conservative esimate for the lifetime of each permeable network would be on the order of a second or so.

We estimate that the fracture in Fig. 5a was open for a slightly longer duration than the connected bubbles in Fig. 5b where nearly all of the particles are incredibly small (~5 μm) and angual. Our thermal calculations suggest that these particles could not have been resident for >0.05 s suggesting a near instanenous injection and quenching process.

For Fig. 5c, we estimate that the network was permeable for ~0.05–0.4 s. The first number represents the time taken to completely sinter and heal basalt, and the latter is the time required to round dacite; both assuming a particle size of ~5 μm which seems to be the approximate average size of the remaining silicic particles.

Appendix 3. Diffusion estimates

Bubble-poor zones next to voids can be interpreted to show areas of diffusive volatile loss into the void-space (Saubin et al., 2016; Webb et al., 2017). The void in Fig. 4b shows a clear zone of bubble-poor glass extending approximately equidistant from the void wall. The average width of the bubble-poor zone is ~80 μm, which can be inferred to represent the volatile diffusion distance. The fact that these fractures have been preserved, suggests that they formed at a relatively shallow level in the conduit, thus is it likely that H_2O will be the predominant species that is diffusing. The diffusivity of H_2O (D) in $m^2\ s^{-1}$ for a basaltic melt of 0.2 wt% H_2O (a reasonable assumption given the measured FTIR concentrations, and assuming our interpretation of shallow level is correct) can be expressed with the following equation from Zhang and Stolper (1991):

$$\ln D = -(12.49 \pm 2.35) - \frac{15200 \pm 3900}{T} \quad (6)$$

where T is temperature in Kelvin, inferred to be 1318 K (1045 °C) based on our oxide thermometry results. Assuming that the opening

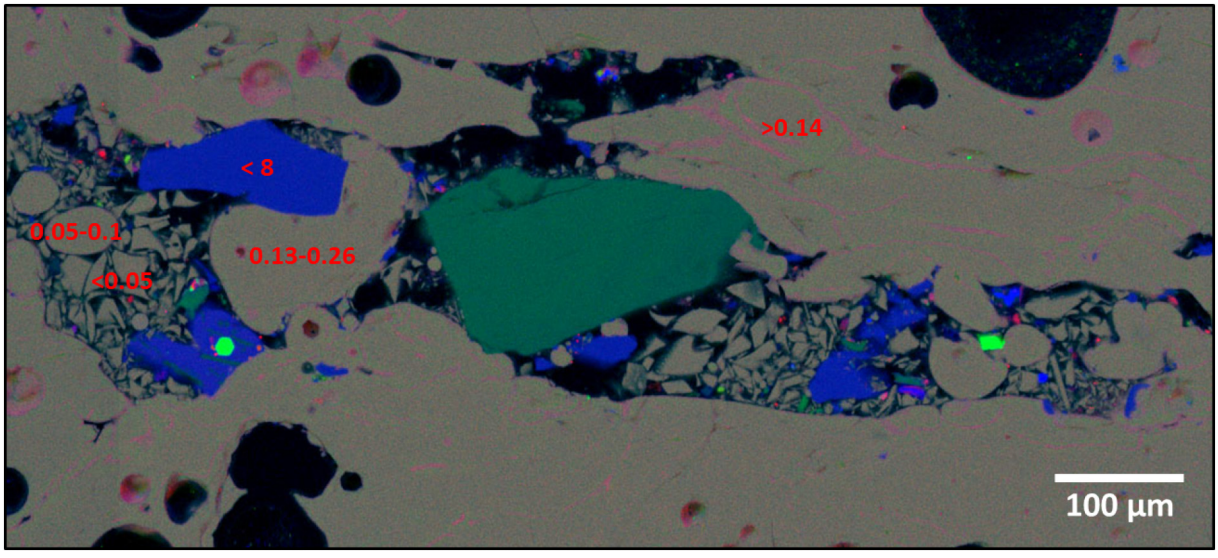

Fig. A6. The compositional map from Fig. 5a, with estimated residence times (in seconds), assuming low H_2O concentrations (consistent with observations) shown in red. (For interpretation of the references to colour in this figure legend, the reader is referred to the web version of this article.)

of a fracture results in disequilibrium within the melt, the H_2O diffusion distance (L) in m, is roughly approximated by the following equation from Zhang and Stolper (1991):

$$L \cong 2\sqrt{Dt} \quad (7)$$

where t is time in seconds. Combining Eqs. (6) and (7), we obtain a diffusion time of ~40s for H_2O to diffuse ~80 μm into the fracture.

References

Adams, N.K., Houghton, B.F., Fagents, S.A., Hildreth, W., 2006. The transition from explosive to effusive eruptive regime: the example of the 1912 Novarupta eruption, Alaska. Geol. Soc. Am. Bull. 118 (5–6), 620–634. https://doi.org/10.1130/b25768.1.

Allard, P., 2010. A CO2-rich gas trigger of explosive paroxysms at Stromboli basaltic volcano, Italy. J. Volcanol. Geotherm. Res. 189 (3–4), 363–374. https://doi.org/10.1016/j.jvolgeores.2009.11.018.

Anderson, S.W., Fink, J.H., 1989. Hydrogen-isotope evidence for extrusion mechanisms of the mount-St-Helens Lava Dome. Nature 341 (6242), 521–523. https://doi.org/10.1038/341521a0.

Anderson, S.W., Fink, J.H., Rose, W.I., 1995. Mount St Helens and Santiaguito lava domes: the effect of short-term eruption rate on surface texture and degassing processes. J. Volcanol. Geotherm. Res. 69 (1–2), 105–116. https://doi.org/10.1016/0377-0273(95)00022-4.

Austin-Erickson, A., Buttner, R., Dellino, P., Ort, M.H., Zimanowski, B., 2008. Phreatomagmatic explosions of rhyolitic magma: Experimental and field evidence. J. Geophys. Res. 113, B11201. https://doi.org/10.1029/2008JB005731.

Bacon, C.R., Hirschmann, M.M., 1988. Mg/Mn partitioning as a test for equilibrium between coexisting Fe-Ti oxides. Am. Mineral. 73, 57–61 (0003-004x/88/0102-0057).

Bagdassarov, N., Dorfman, A., Dingwell, D.B., 2000. Effect of alkalis, phosphorus, and water on the surface tension of haplogranite melt. Am. Mineral. 85 (1), 33–40. https://doi.org/10.2138/am-2000-0105.

Berlo, K., Tuffen, H., Smith, V.C., Castro, J.M., Pyle, D.M., Mather, T.A., Geraki, K., 2013. Element variations in rhyolitic magma resulting from gas transport. Geochim. Cosmochim. Acta 121, 436–451. https://doi.org/10.1016/j.gca.2013.07.032.

Blundy, J., Cashman, K., 2008. Petrologic reconstruction of magmatic system variables and processes. Miner. Incl. Volcanic Process. 69 (1), 179–239. https://doi.org/10.2138/rmg.2008.69.6.

Blundy, J., Cashman, K., Humphreys, M., 2006. Magma heating by decompression-driven crystallization beneath andesite volcanoes. Nature 443 (7107), 76–80. https://doi.org/10.1038/nature05100.

Bottinga, Y., Weill, D.F., 1970. Densities of liquid silicate systems calculated from partial molar volumes of oxide components. Am. J. Sci. 269 (2), 169–182. https://doi.org/10.2475/ajs.269.2.169.

Budd, D.A., Troll, V.R., Dahren, B., Burchardt, S., 2016. Persistent multitiered magma plumbing beneath Katla volcano, Iceland. Geochem. Geophys. Geosyst. 17 (3), 966–980. https://doi.org/10.1002/2015GC006118.

Castro, J.M., Dingwell, D.B., 2009. Rapid ascent of rhyolitic magma at Chaiten volcano, Chile. Nature 461 (7265), 780–U729. https://doi.org/10.1038/nature08458.

Castro, J.M., Cordonnier, B., Tuffen, H., Tobin, M., Puskar, L., Martin, M.C., Bechtel, B., 2012. The role of melt-fracture degassing in defusing explosive rhyolite eruptions at volcán Chaitén. Earth Planet. Sci. Lett. 333-334, 63–69. https://doi.org/10.1016/j.epsl.2012.04.024.

Denton, J.S., Tuffen, H., Gilbert, J.S., Odling, N., 2009. The hydration and alteration of perlite and rhyolite. J. Geol. Soc. Lond. 166, 895–904. https://doi.org/10.1144/0016-76492008-007.

Dixon, J.E., Stolper, E., Delaney, J.R., 1988. Infrared spectroscopic measurements of Co2 and H2o in Juan-De-Fuca Ridge basaltic glasses. Earth Planet. Sci. Lett. 90 (1), 87–104. https://doi.org/10.1016/0012-821X(88)90114-8.

Duller, R.A., Mountney, N.P., Russell, A.J., Cassidy, N.C., 2008. Architectural analysis of a volcaniclastic jökulhlaup deposit, southern Iceland: sedimentary evidence for supercritical flow. Sedimentology 55 (4), 939–964. https://doi.org/10.1111/j.1365-3091.2007.00931.x.

Edmonds, M., Gerlach, T.M., 2007. Vapor segregation and loss in basaltic melts. Geology 35 (8), 751–754. https://doi.org/10.1130/g23464a.1.

Eichelberger, J.C., Carrigan, C.R., Westrich, H.R., Price, R.H., 1986. Non-explosive silicic volcanism. Nature 323 (6089), 598–602. https://doi.org/10.1038/323598a0.

Eppelbaum, L., Kutasov, I., Pilchin, A., 2014. Thermal Properties of Rocks and Density of Fluids, Applied Geothermics. Springer-Verlag, Berlin Heidelberg. https://doi.org/10.1007/978-3-642-34023-9_2.

Farquharson, J.I., Wadsworth, F.B., Heap, M.J., Baud, P., 2017. Time-dependent permeability evolution in compacting volcanic fracture systems and implications for gas overpressure. J. Volcanol. Geotherm. Res. 339, 81–97. https://doi.org/10.1016/j.jvolgeores.2017.04.025.

Gardner, J.E., Denis, M.-H., 2004. Heterogeneous bubble nucleation on Fe-Ti oxide crystals in high-silica rhyolitic melts1. Geochim. Cosmochim. Acta 68 (17), 3587–3597. https://doi.org/10.1016/j.gca.2004.02.021.

Gardner, J.E., Ketcham, R.A., 2011. Bubble nucleation in rhyolite and dacite melts: temperature dependence of surface tension. Contrib. Mineral. Petrol. 162 (5), 929–943. https://doi.org/10.1007/s00410-011-0632-5.

Gardner, J.E., Ketcham, R.A., Moore, G., 2013. Surface tension of hydrous silicate melts: constraints on the impact of melt composition. J. Volcanol. Geotherm. Res. 267, 68–74. https://doi.org/10.1016/j.jvolgeores.2013.09.007.

Gardner, J.E., Llewellin, E.W., Watkins, J.M., Befus, K.S., 2017. Formation of obsidian pyroclasts by sintering of ash particles in the volcanic conduit. Earth Planet. Sci. Lett. 459, 252–263. https://doi.org/10.1016/j.epsl.2016.11.037.

Gaunt, H.E., Sammonds, P.R., Meredith, P.G., Smith, R., Pallister, J.S., 2014. Pathways for degassing during the lava dome eruption of Mount St. Helens 2004–2008. Geology 42 (11), 947–950. https://doi.org/10.1130/g35940.1.

Ghiorso, M.S., Evans, B.W., 2008. Thermodynamics of rhombohedral oxide solid solutions and a revision of the Fe-Ti two-oxide geothermometer and oxygen-barometer. Am. J. Sci. 308, 957–1039. https://doi.org/10.2475/09.2008.01.

Giordano, D., Dingwell, D.B., 2003. Viscosity of hydrous Etna basalt: implications for Plinian-style basaltic eruptions. Bull. Volcanol. 65 (1), 8–14. https://doi.org/10.1007/s00445-002-0233-2.

Giordano, D., Russell, J.K., Dingwell, D.B., 2008. Viscosity of magmatic liquids: a model. Earth Planet. Sci. Lett. 271 (1–4), 123–134. https://doi.org/10.1016/j.epsl.2008.03.038.

Gonnermann, H.M., Manga, M., 2005. Nonequilibrium magma degassing: results from modeling of the ca. 1340 A.D. eruption of Mono Craters, California. Earth Planet. Sci. Lett. 238 (1–2), 1–16. https://doi.org/10.1016/j.epsl.2005.07.021.

Gudmundsson, M.T., 2013. Melting of Ice by magma-ice-water interactions during subglacial eruptions as an indicator of heat transfer in subaqueous eruptions, explosive subaqueous volcanism. Am. Geophys. Union, 61–72 https://doi.org/10.1029/140GM04.

Gudmundsson, M.T., Sigmundsson, F., Bjornsson, H., 1997. Ice-volcano interaction of the 1996 Gjalp subglacial eruption, Vatnajokull, Iceland. Nature 389 (6654), 954–957. https://doi.org/10.1038/40122.

Hayward, C., 2011. High spatial resolution electron probe microanalysis of tephras and melt inclusions without beam-induced chemical modification. The Holocene 22 (1), 119–125. https://doi.org/10.1177/0959683611409777.

Hoblitt, R.P., Harmon, R.S., 1993. Bimodal density distribution of cryptodome dacite from the 1980 eruption of Mount St. Helens, Washington. Bull. Volcanol. 55, 421–437. https://doi.org/10.1007/BF00302002.

Hoskuldsson, A., Sparks, R.S.J., 1997. Thermodynamics and fluid dynamics of effusive subglacial eruptions. Bull. Volcanol. 59 (3), 219–230. https://doi.org/10.1007/s004450050187.

Houghton, B.F., Gonnermann, H.M., 2008. Basaltic explosive volcanism: constraints from deposits and models. Chem. Erde-Geochem. 68 (2), 117–140. https://doi.org/10.1016/j.chemer.2008.04.002.

Humphreys, M.C.S., Edmonds, M., Christopher, T., Hards, V., 2009. Chlorine variations in the magma of Soufrière Hills Volcano, Montserrat: insights from Cl in hornblende and melt inclusions. Geochim. Cosmochim. Acta 73 (19), 5693–5708. https://doi.org/10.1016/j.gca.2009.06.014.

Jaupart, C., 1998. Gas loss from magmas through conduit walls during eruption. In: Gilbert, J.S., Sparks, R.S.J. (Eds.), The Physics of Explosive Volcanic Eruptions. Geological Society Special Publication, No. 145, pp. 73–90 https://doi.org/10.1144/gsl.sp.1996.145.01.05.

Jaupart, C., Allègre, C.J., 1991. Gas content, eruption rate and instabilities of eruption regime in silicic volcanoes. Earth Planet. Sci. Lett. 102 (3–4), 413–429. https://doi.org/10.1016/0012-821x(91)90032-d.

Jóhannesson, H., Sæmundsson, K., 2014. Geological Map of Iceland. Bedrock Geology.1: 600,000. Icelandic Institute of Natural History.

Kendrick, J.E., Lavallée, Y., Varley, N., Wadsworth, F.B., Lamb, O.D., Vasseur, J., 2016. Blowing off steam: Tuffisite formation as a regulator for lava dome eruptions. Front. Earth Sci. 4. https://doi.org/10.3389/feart.2016.00041.

Klug, C., Cashman, K.V., 1996. Permeability development in vesiculating magmas: implications for fragmentation. Bull. Volcanol. 58 (2), 87–100. https://doi.org/10.1007/s004450050128.

Kolzenburg, S., Heap, M.J., Lavallée, Y., Russell, J.K., Meredith, P.G., Dingwell, D.B., 2012. Strength and permeability recovery of tuffisite-bearing andesite. Solid Earth 3 (2), 191–198. https://doi.org/10.5194/se-3-191-2012.

Lacasse, C., Sigurdsson, H., Jóhannesson, H., Paterne, M., Carey, S., 1995. Source of Ash Zone 1 in the North Atlantic. Bull. Volcanol. 57 (1), 18–32. https://doi.org/10.1007/bf00298704.

Lacasse, C., Sigurdsson, H., Carey, S.N., Jóhannesson, H., Thomas, L.E., Rogers, N.W., 2007. Bimodal volcanism at the Katla subglacial caldera, Iceland: insight into the geochemistry and petrogenesis of rhyolitic magmas. Bull. Volcanol. 69 (4), 373–399. https://doi.org/10.1007/s00445-006-0082-5.

Larsen, G., 2000. Holocene eruptions within the Katla volcanic system, south Iceland: characteristics and environmental impact. Jökull 49, 1–28.

Larsen, G., 2010. 3 Katla: tephrochronology and eruption history. In: Anders Schomacker, J.K., Kurt, H.K. (Eds.), Developments in Quaternary Science. Elsevier, pp. 23–49 https://doi.org/10.1016/s1571-0866(09)01303-7.

Larsen, G., Newton, A.J., Dugmore, A.J., Vilmundardóttir, E.G., 2001. Geochemistry, dispersal, volumes and chronology of Holocene silicic tephra layers from the Katla volcanic system, Iceland. J. Quat. Sci. 16 (2), 119–132. https://doi.org/10.1002/jqs.587.

Larsen, G., Eiríksson, J., Gudmundsdóttir, E.R., 2014. Last millennium dispersal of air-fall tephra and ocean-rafted pumice towards the north Icelandic shelf and the Nordic seas. Geol. Soc. Lond., Spec. Publ. 398 (1), 113–140. https://doi.org/10.1144/sp398.4.

Maizels, J., 1992. Boulder ring structures produced during Jökulhlaup flows. Origin and hydraulic significance. Geogr. Ann. Ser. A Phys. Geogr. 74 (1), 21–33. https://doi.org/10.2307/521467.

Maizels, J., 1993. Lithofacies variations within sandur deposits: the role of runoff regime, flow dynamics and sediment supply characteristics. Sediment. Geol. 85 (1), 299–325. https://doi.org/10.1016/0037-0738(93)90090-R.

Mangan, M., Sisson, T., 2005. Evolution of melt-vapor surface tension in silicic volcanic systems: experiments with hydrous melts. J. Geophys. Res. Solid Earth 110 (B1). https://doi.org/10.1029/2004JB003215 n/a-n/a.

Martel, C., Pichavant, M., Bourdier, J.L., Traineau, H., Holtz, F., Scaillet, B., 1998. Magma storage conditions and control of eruption regime in silicic volcanoes: experimental evidence from Mt. Pelée. Earth Planet. Sci. Lett. 156 (1–2), 89–99. https://doi.org/10.1016/s0012-821x(98)00003-x.

Menand, T., Phillips, J.C., 2007. Gas segregation in dykes and sills. J. Volcanol. Geotherm. Res. 159 (4), 393–408. https://doi.org/10.1016/j.jvolgeores.2006.08.003.

Moore, G., Vennemann, T., Carmichael, I.S.E., 1998. An empirical model for the solubility of H_2O in magmas to 3 kilobars. Am. Mineral. 83 (1–2), 36–42. https://doi.org/10.2138/am-1998-1-203.

Morrissey, M., Zimanowski, B., Wohletz, K., Buettner, R., 2000. Phreatomagmatic fragmentation. In: Sigurdsson, H. (Ed.), Encyclopedia of Volcanoes. Academic Pres, San Diego, pp. 431–445.

Nakada, S., Uto, K., Sakuma, S., Eichelberger, J., Shimizu, H., 2005. Scientific results of conduit drilling in the Unzen scientific drilling project (USDP). Sci. Drill. 1, 18–22. https://doi.org/10.2204/iodp.sd.1.03.2005.

Namiki, A., Manga, M., 2008. Transition between fragmentation and permeable outgassing of low viscosity magmas. J. Volcanol. Geotherm. Res. 169 (1–2), 48–60. https://doi.org/10.1016/j.jvolgeores.2007.07.020.

Newman, S., Lowenstern, J.B., 2002. VolatileCalc: a silicate melt–H2O_CO2 so₁ution model written in visual basic for excel. Comput. Geosci. 28 (5), 597–604. https://doi.org/10.1016/s0098-3004(01)00081-4.

Newton, A., 1999. Ocean-transported Pumice in the North Atlantic. (PhD thesis Thesis). University of Edinburgh.

Noguchi, S., Toramaru, A., Nakada, S., 2008. Groundmass crystallization in dacite dykes taken in Unzen Scientific Drilling Project (USDP-4). J. Volcanol. Geotherm. Res. 175 (1–2), 71–81. https://doi.org/10.1016/j.jvolgeores.2008.03.037.

O'Connor, J.E., Costa, J.E., 2004. The World's Largest Floods, Past and Present: Their Causes and Magnitudes. U.S. Geological Survey, University of Minnesota.

Óladóttir, B.A., Larsen, G., Þórðarson, Þ., Sigmarsson, O., 2005. The Katla volcano S-Iceland: Holocene tephra stratigraphy and eruption frequency. Jökull 55, 53–74.

Óladóttir, B., Sigmarsson, O., Larsen, G., Thordarson, T., 2008. Katla volcano, Iceland: magma composition, dynamics and eruption frequency as recorded by Holocene tephra layers. Bull. Volcanol. 70 (4), 475–493. https://doi.org/10.1007/s00445-007-0150-5.

Owen, J., 2016. Using volatiles in magma to decipher subglacial eruption dynamics. Geol. Today 32 (1), 30–37. https://doi.org/10.1111/gto.12127.

Owen, J., Tuffen, H., McGarvie, D.W., 2012. Using dissolved H_2O in rhyolitic glasses to estimate palaeo-ice thickness during a subglacial eruption at Bláhnúkur (Torfajökull, Iceland). Bull. Volcanol. 74 (6), 1355–1378. https://doi.org/10.1007/s00445-012-0601-5.

Owen, J., Tuffen, H., McGarvie, D.W., 2013a. Explosive subglacial rhyolitic eruptions in Iceland are fuelled by high magmatic H2O and closed-system degassing. Geology 41 (2), 251–254. https://doi.org/10.1130/G33647.1.

Owen, J., Tuffen, H., McGarvie, D.W., 2013b. Pre-eruptive volatile content, degassing paths and depressurisation explaining the transition in style at the subglacial rhyolitic eruption of Dalakvísl, South Iceland. J. Volcanol. Geotherm. Res. 258, 143–162. https://doi.org/10.1016/j.jvolgeores.2013.03.021.

Owen, J., Shea, T., Tuffen, H., 2017. The role of bubbles during the 1918 subglacial basalt eruption of Katla, south Iceland. Joint Assembly TSG-VMSG-BGA. University of Liverpool, p. 163.

Owen, J., Tuffen, H., McGarvie, D., 2018. Magma degassing in the effusive-explosive subglacial rhyolitic eruption of Dalakvísl, Torfajökull, Iceland: insights into quenching pressures, palaeo-ice thickness, and edifice erosion. Jökull (68) (in press).

Papale, P., 1999. Strain-induced magma fragmentation in explosive eruptions. Nature 397, 425–428. https://doi.org/10.1038/17109.

Phillips, J.C., Lane, S.J., Lejeune, A.-M., Hilton, M., 1995. Gum rosin-acetone system as an analogue to the degassing behaviour of hydrated magmas. Bull. Volcanol. 57 (4), 263–268. https://doi.org/10.1007/bf00265425.

Plail, M., Edmonds, M., Humphreys, M.C.S., Barclay, J., Herd, R.A., 2014. Geochemical evidence for relict degassing pathways preserved in andesite. Earth Planet. Sci. Lett. 386, 21–33. https://doi.org/10.1016/j.epsl.2013.10.044.

Pope, R., 2015. Sintering of fragmented rhyolitic magma in the Cordón Caulle vent, Chile. (MSc thesis Thesis). Lancaster University.

Proussevitch, A.A., Sahagian, D.L., 1996. Dynamics of coupled diffusive and decompressive bubble growth in magmatic systems. J. Geophys. Res. Solid Earth 101 (B8), 17447–17455. https://doi.org/10.1029/96JB01342.

Ristić, M.M., Milosević, S., 2006. Frenkel's theory of sintering. Sci. Sinter. 38 (1), 7–11. https://doi.org/10.2298/SOS0601007R.

Russell, A.J., Duller, R., Mountney, N.P., 2010. 11 volcanogenic Jökulhlaups (glacier outburst floods) from Mýrdalsjökull: impacts on proglacial environments. In: Anders Schomacker, J.K., Kurt, H.K. (Eds.), Developments in Quaternary Science. Elsevier, pp. 181–207 https://doi.org/10.1016/s1571-0866(09)01311-6.

Rust, A.C., Cashman, K.V., Wallace, P.J., 2004. Magma degassing buffered by vapor flow through brecciated conduit margins. Geology 32 (4), 349–352. https://doi.org/10.1130/g20388.2.

Saubin, E., Tuffen, H., Gurioli, L., Owen, J., Castro, J.M., Berlo, K., McGowan, E., Schipper, C.I., Wehbe, K., 2016. Conduit dynamics in transitional rhyolitic activity recorded by tuffisite vein textures from the 2008–2009 Chaitén eruption. Front. Earth Sci. 4. https://doi.org/10.3389/feart.2016.00059.

Schipper, C.I., Castro, J.M., Tuffen, H., James, M.R., How, P., 2013. Shallow vent architecture during hybrid explosive–effusive activity at Cordón Caulle (Chile, 2011–12): evidence from direct observations and pyroclast textures. J. Volcanol. Geotherm. Res. 262 (0), 25–37. https://doi.org/10.1016/j.jvolgeores.2013.06.005.

Shea, T., Hellebrand, E., Gurioli, L., Tuffen, H., 2014. Conduit- to Localized-scale Degassing during Plinian Eruptions: Insights from Major Element and Volatile (Cl and H2O) analyses within Vesuvius ad 79 Pumice. J. Petrol. 55 (2), 315–344. https://doi.org/10.1093/petrology/egt069.

Smithsonian, 2016. Katla. http://volcano.si.edu/volcano.cfm?vn=372030 (04/04/16).

Sparks, R.S.J., 1978. The dynamics of bubble formation and growth in Magmas - review and analysis. J. Volcanol. Geotherm. Res. 3 (1–2), 1–37. https://doi.org/10.1016/0377-0273(78)90002-1.

Sparks, R.S.J., 1997. Causes and consequences of pressurisation in lava dome eruptions. Earth Planet. Sci. Lett. 150, 177–189. https://doi.org/10.1016/S0012-821X(97)00109-X.

Stasiuk, M.V., Barclay, J., Carroll, M.R., Jaupart, C., Ratte, J.C., Sparks, R.S.J., Tait, S.R., 1996. Degassing during magma ascent in the Mule Creek vent (USA). Bull. Volcanol. 58 (2–3), 117–130. https://doi.org/10.1007/s004450050130.

Stolper, E., 1982. Water in silicate-glasses: an infrared spectroscopic study. Contrib. Mineral. Petrol. 81 (1), 1–17. https://doi.org/10.1007/BF00371154.

Sturkell, E., Einarsson, P., Sigmundsson, F., Hooper, A., Ófeigsson, B.G., Geirsson, H., Ólafsson, H., 2010. 2 katla and Eyjafjallajökull volcanoes. In: Anders Schomacker, J.K., Kurt, H.K. (Eds.), Developments in Quaternary Science. Elsevier, pp. 5–21 https://doi.org/10.1016/s1571-0866(09)01302-5.

Sumner, J.M., Blake, S., Matela, R.J., Wolff, J.A., 2005. Spatter. J. Volcanol. Geotherm. Res. 142 (1–2), 49–65. https://doi.org/10.1016/j.jvolgeores.2004.10.013.

Taniguchi, H., 1988. Surface tension of melts in the system CaMgSi2O6-CaAl2Si2O8 and its structural significance. Contrib. Mineral. Petrol. 100 (4), 484–489. https://doi.org/10.1007/bf00371377.

Tómasson, H., 1996. The jökulhlaup from Katla in 1918. Ann. Glaciol. 22, 249–254. https://doi.org/10.1017/S0260305500015494.

Tuffen, H., Castro, J.M., 2009. The emplacement of an obsidian dyke through thin ice: Hrafntinnuhryggur, Krafla Iceland. J. Volcanol. Geotherm. Res. 185 (4), 352–366. https://doi.org/10.1016/j.jvolgeores.2008.10.021.

Tuffen, H., Dingwell, D.B., 2005. Fault textures in volcanic conduits: evidence for seismic trigger mechanisms during silicic eruptions. Bull. Volcanol. 67, 370–387. https://doi.org/10.1007/s00445-004-0383-5.

Tuffen, H., Dingwell, D.B., Pinkerton, H., 2003. Repeated fracture and healing of silicic magma generate flow banding and earthquakes? Geology 31, 1089–1092. https://doi.org/10.1130/G19777.1.

Tuffen, H., Owen, J., Denton, J., 2010. Magma degassing during subglacial eruptions and its use to reconstruct palaeo-ice thicknesses. Earth Sci. Rev. 99 (1–2), 1–18. https://doi.org/10.1016/j.earscirev.2010.01.001.

Uhlmann, D., Klein, L., Onorato, P., Hopper, R., 1975. The formation of lunar breccias-Sintering and crystallization kinetics. Lunar and Planetary Science Conference Proceedings, pp. 693–705.

Vasseur, J., Wadsworth, F.B., Lavallée, Y., Hess, K.-U., Dingwell, D.B., 2013. Volcanic sintering: timescales of viscous densification and strength recovery. Geophys. Res. Lett. 40 (21), 5658–5664. https://doi.org/10.1002/2013GL058105.

Vergniolle, S., Jaupart, C., 1986. Separated two-phase flow and basaltic eruptions. J. Geophys. Res. Solid Earth 91 (B12), 12842–12860. https://doi.org/10.1029/JB091iB12p12842.

Villemant, B., Boudon, G., 1998. Transition from dome-forming to plinian eruptive styles controlled by H_2O and Cl degassing. Nature 392 (6671), 65–69. https://doi.org/10.1038/32144.

Villemant, B., Boudon, G., 1999. H_2O and halogen (F, Cl, Br) behaviour during shallow magma degassing processes. Earth Planet. Sci. Lett. 168 (3–4), 271–286. https://doi.org/10.1016/s0012-821x(99)00058-8.

Villemant, B., Boudon, G., Nougrigat, S., Poteaux, S., Michel, A., 2003. Water and halogens in volcanic clasts: tracers of degassing processes during Plinian and dome-building eruptions. In: Oppenheimer, C., Pyle, D.M., Barclay, J. (Eds.), Geol Soc Spec Publ. vol. 213. Geological Society London, Special Publications, pp. 63–79. https://doi.org/10.1144/gsl.sp.2003.213.01.05.

Villemant, B., Mouatt, J., Michel, A., 2008. Andesitic magma degassing investigated through H_2O vapour-melt partitioning of halogens at Soufriere Hills Volcano, Montserrat (Lesser Antilles). Earth Planet. Sci. Lett. 269 (1–2), 212–229. https://doi.org/10.1016/j.epsl.2008.02.014.

Vosteen, H.-D., Schellschmidt, R., 2003. Influence of temperature on thermal conductivity, thermal capacity and thermal diffusivity for different types of rock. Phys. Chem. Earth A/B/C 28 (9–11), 499–509. https://doi.org/10.1016/S1474-7065(03)00069-X.

Walker, D., Mullins, O., 1981. Surface tension of natural silicate melts from 1,200°–1,500 °C and implications for melt structure. Contrib. Mineral. Petrol. 76 (4), 455–462. https://doi.org/10.1007/bf00371487.

Webb, C., Tuffen, H., Owen, J., Castro, J., Berlo, K., Schipper, C.I., Wehbe, K., 2017. Mid-loaf crisis: internal breadcrust surfaces in rhyolitic bombs from Chaitén. IAVCEI 2017 Scientific Assembly, Portland, Oregon, U.S.A.

Westrich, H.R., Eichelberger, J.C., 1994. Gas transport and bubble collapse in rhyolitic magma: an experimental approach. Bull. Volcanol. 56 (6–7), 447–458. https://doi.org/10.1007/BF00302826.

Whittington, A.G., Hofmeister, A.M., Nabelek, P.I., 2009. Temperature-dependent thermal diffusivity of the Earth's crust and implications for magmatism. Nature 458 (7236), 319–321. https://doi.org/10.1038/nature07818.

Wilson, L., 1980. Relationships between pressure, volatile content and ejecta velocity in three types of volcanic explosion. J. Volcanol. Geotherm. Res. 8 (2–4), 297–313. https://doi.org/10.1016/0377-0273(80)90110-9.

Wilson, L., Head, J.W., 2002. Heat transfer and melting in subglacial basaltic volcanic eruptions: implications for volcanic deposit morphology and meltwater volumes. Geol. Soc. Lond., Spec. Publ. 202 (1), 5–26. https://doi.org/10.1144/gsl.sp.2002.202.01.02.

Wilson, L., Mouginis-Mark, P.J., 2003. Phreatomagmatic explosive origin of Hrad Vallis, Mars. J. Geophys. Res. Planets 108 (E8). https://doi.org/10.1029/2002JE001927 (n/a-n/a).

Woodcock, D.C., Lane, S.J., Gilbert, J.S., 2014. Ice-melt rates in liquid-filled cavities during explosive subglacial eruptions. J. Geophys. Res. Solid Earth 119 (3), 1803–1817. https://doi.org/10.1002/2013JB010617.

Woodcock, D.C., Gilbert, J.S., Lane, S.J., 2015. Ice-melt rates by steam condensation during explosive subglacial eruptions. J. Geophys. Res. Solid Earth 120 (2), 864–878. https://doi.org/10.1002/2014JB011619.

Woodcock, D.C., Lane, S.J., Gilbert, J.S., 2016. Ice-melt rates during volcanic eruptions within water-drained, low-pressure subglacial cavities. J. Geophys. Res. Solid Earth 121 (2), 648–662. https://doi.org/10.1002/2015JB012036.

Yokoyama, T., Okumura, S., Nakashima, S., 2008. Hydration of rhyolitic glass during weathering as characterized by IR microspectroscopy. Geochim. Cosmochim. Acta 72 (1), 117–125. https://doi.org/10.1016/j.gca.2007.10.018.

Zhang, Y., Stolper, E.M., 1991. Water diffusion in a basaltic melt. Nature 351 (6324), 306–309. https://doi.org/10.1038/351306a0.

Zimanowski, B., Fröhlich, G., Lorenz, V., 1991. Quantitative experiments on phreatomagmatic explosions. J. Volcanol. Geotherm. Res. 48 (3–4), 341–358. https://doi.org/10.1016/0377-0273(91)90050-a.